

OBSERVABILITY ANALYSIS AND OPTIMIZATION FOR ANGLES-ONLY NAVIGATION OF DISTRIBUTED SPACE SYSTEMS

Justin Kruger*, Simone D’Amico†

Angles-only navigation methods are compelling for distributed space systems (DSS) such as swarms and constellations. However, complex dependencies between state observability and system parameters present a challenging design problem. This paper proposes a unified angles-only observability analysis and design framework enabling designers of a DSS to 1) analytically determine whether its orbit state is observable, 2) numerically estimate its expected navigation performance, and 3) intelligently optimize the system to meet navigation requirements. First, a new system measurement topology representation is proposed for which analytic orbit observability can be assessed via a set of graphical conditions. Second, methods for numeric estimation of the achievable state covariance are augmented with auxiliary state variables, dynamics uncertainty, and measurement availability constraints. Third, a system cost function is developed and the topological and numeric methods are placed within a quasi-Newton optimization framework to enable automatic system design. The optimization is applied to a distributed science swarm and a space situational awareness constellation in lunar orbit. Both scenarios converge to a global cost minimum and output designs that achieve user requirements under realistic measurement conditions and constraints. Combined analytic and numeric methods therefore presents a powerful tool for design of angles-only DSS.

keywords: angles-only navigation, vision-based navigation, observability analysis, design optimization

1. Introduction

Angles-only methods, in which observer spacecraft obtain bearing angles to target space objects using on-board vision-based sensors (VBS), are compelling for navigation of distributed space systems (DSS). Typical DSS in Earth orbit rely on external Global Navigation Satellite System (GNSS) measurements for navigation, whereas DSS in deep space often employ radio localization via ground-based resources such as the NASA Deep Space Network (DSN). However, GNSS cannot be applied in signal-denied scenarios of interest, and DSN usage is not easily scalable to future distributed missions [1]. In contrast, angles-only navigation is primarily autonomous, self-contained, and leverages only on-board resources. Cameras are robust, low cost, low power sensors already present on most spacecraft, possessing high dynamic range and small form factors conducive to accurate navigation and spacecraft miniaturization. Cameras may also obtain passive measurements to non-cooperative or unidentified targets, particularly useful in space domain awareness (SDA). Many DSS proposals therefore present angles-only navigation as a central aspect [2–7].

As documented in literature, two flight experiments have demonstrated angles-only navigation in orbit.

In 2012, the Advanced Rendezvous using GPS and Optical Navigation (ARGON) experiment enabled the rendezvous of two smallsats in low Earth orbit (LEO) from inter-satellite separations of 30km to 3km [8]. In 2016, the Autonomous Vision Approach Navigation and Target Identification (AVANTI) experiment similarly conducted a rendezvous between a mother-ship smallsat and deployed picosatellite from separations of 13km to 50m [6]. More recently, Stanford’s Space Rendezvous Laboratory has developed the Absolute and Relative Trajectory Measurement System (ARTMS) [3, 9]. ARTMS is a self-contained software payload that provides distributed, autonomous angles-only navigation for DSS orbiting an arbitrary central body. ARTMS will be flight tested in 2022 as part of the NASA Starling mission, a swarm technology demonstration consisting of four CubeSats in LEO [5]. Usage of ARTMS in lunar and Martian orbits has also been studied [4, 10].

A key design challenge for angles-only navigation is weak observability of target range. Bearing angles do not provide explicit range information and multiple cooperative observers in a system are necessary to achieve complete state observability and long-term convergence [3, 11–13]. System properties such as orbit geometry, sensor quality, measurement availability and communication topology can affect observability significantly and unpredictably. Angles-only observability has therefore been extensively studied.

*Stanford University, USA, jkruger@stanford.edu

†Stanford University, USA, damicos@stanford.edu

2. Background

Existing results can be broadly categorized into four areas: treatment of two- or three-spacecraft systems [11, 12, 14] or larger systems [4, 10, 13, 15], and usage of analytic observability methods [12–14] such as Lie derivatives or numeric observability methods [4, 10, 11, 15] such as covariance estimation. Despite this, comparatively little attention has been paid to how angles-only systems may be practically designed to achieve required navigation performance for a scenario. If ARTMS or similar architectures are to be applied to future missions, it is necessary to 1) determine whether complete observability can be achieved using angles-only measurements in the desired scenario; 2) given a system configuration, compute expected navigation performance and assess whether requirements are met; 3) intelligently design a system and optimize its parameters to achieve navigation requirements at minimal cost. Although some authors have applied optimization techniques to broader spacecraft or mission design [16], explicit navigation constraints are often untreated and have not been studied in this context. Furthermore, prior analytic and numeric results have not addressed several critical design aspects, including partial or non-global measurement availability [12]; dynamics model uncertainties [11]; and consistency of observability across varying topologies, geometries, and state variables.

In response, this paper constructs a new, unified angles-only observability analysis and design framework from three interrelated components: analytic observability analysis, numeric observability analysis, and design optimization. First, a modified graph topology representation is introduced for DSS. For a more realistic treatment of distribution, the topology does not assume global measurement availability and adopts weighted and self-loop edges to better characterize the flow of measurement information. Sufficient conditions to ensure analytic graph observability are provided by applying prior Lie derivative results to the new topology. Second, a modified numeric method for observability analysis is presented. Measurement sensitivity and noise matrices are used to estimate achievable state uncertainty from a simulated measurement batch. Added aspects include the effects of dynamics uncertainty, partial target visibility, and auxiliary state estimation. The numeric method is used to validate the topological conditions. Third, an optimization framework is fused with the analytic and numeric approaches. A quadratic objective function is developed to balance navigation performance (as computed via the above methods) with overall system costs. Quasi-Newton methods

are applied to minimize the objective and automatic optimization is explored for two case studies in lunar orbit: a distributed science swarm and an SSA constellation. More generally, by combining these tools, designers are able to quickly determine whether a system is observable, estimate expected navigation performance, and intelligently optimize it to fulfil requirements.

Following this introduction, Section 2 introduces relevant mathematical modeling. Section 3 presents a graph topology representation for DSS and sufficient topological conditions for orbit observability. Section 4 presents numeric methods for system observability analysis and associated results. Section 5 presents an optimization framework for angles-only observability and its application to two case studies. Section 6 concludes the paper.

2. Background

2.1 Terminology

A DSS consists of all resident space objects (RSO) whose states are to be estimated. ‘Active’ objects are observer spacecraft with an onboard VBS which actively obtain measurements and perform navigation, whereas ‘passive’ objects do not perform navigation but may be tracked by active observers. To enable cooperative navigation, observers broadcast their absolute orbit estimate and bearing angle measurements to other observers over an inter-satellite link (ISL). Each observer is therefore in contact with a set of ‘remote’ ISL observers and has access to remote measurements of system objects.

Navigation is decentralized in that each observer only estimates the states of those RSO in its ‘subsystem’. A subsystem consists of the ‘local’ observer, all targets visible to its VBS, and remote observers which 1) share a target with the local observer; 2) are a target of the local observer; 3) are measuring the local observer; or 4) are measuring a remote observer which fulfils conditions 1), 2) or 3). In this fashion, global communication is not required and observers only process measurement information relevant to themselves or their visible targets. Furthermore, measurement and navigation tasks are distributed to both improve DSS coverage and reduce on-board computation costs.

‘Beacon’ objects are able to observe their own absolute orbit, either via ‘external’ measurement sources such as GNSS or ‘internal’ measurement sources such as inter-satellite bearing angles. Figure 1 presents a notional illustration of these terms.

2.2 Coordinate Frames

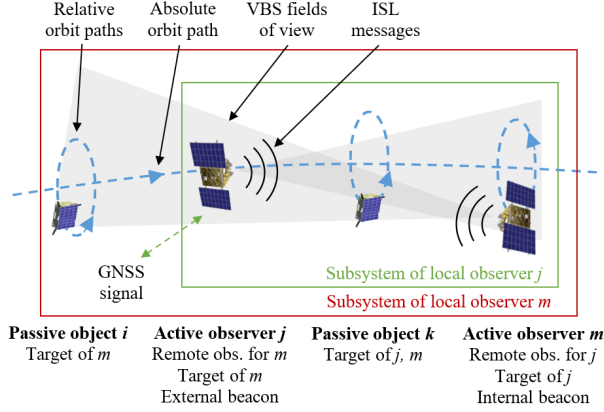


Fig. 1: An illustration of a four-member subsystem with two active observers and two passive RSO.

2.2 Coordinate Frames

Spacecraft states are modeled in an inertial reference frame centered on an arbitrary central body, denoted \mathcal{I} (commonly a planet-centered, moon-centered or Sun-centered frame). Two rotating frames are also defined. First, consider the radial/along-track/cross-track (RTN) frame of an observer spacecraft, denoted \mathcal{R} . It is centered on and rotates with the observer and consists of orthogonal basis vectors $\hat{\mathbf{x}}^{\mathcal{R}}$ (directed along the observer's absolute position vector); $\hat{\mathbf{z}}^{\mathcal{R}}$ (directed along the observer's orbital angular momentum vector); and $\hat{\mathbf{y}}^{\mathcal{R}} = \hat{\mathbf{z}}^{\mathcal{R}} \times \hat{\mathbf{x}}^{\mathcal{R}}$ [17]. Similarly, define a frame \mathcal{W} using $\hat{\mathbf{y}}^{\mathcal{W}}$ (directed along the observer's velocity vector); $\hat{\mathbf{z}}^{\mathcal{W}} = \hat{\mathbf{z}}^{\mathcal{R}}$; and $\hat{\mathbf{x}}^{\mathcal{W}} = \hat{\mathbf{y}}^{\mathcal{W}} \times \hat{\mathbf{z}}^{\mathcal{W}}$. \mathcal{W} only differs from \mathcal{R} by a rotation of the observer flight path angle ϕ_f about $\hat{\mathbf{z}}^{\mathcal{R}}$ with $\phi_f \approx 0$ in near-circular orbits [17]. Finally, define the observer VBS coordinate frame, consisting of orthogonal basis vectors $\hat{\mathbf{x}}^{\mathcal{V}}, \hat{\mathbf{y}}^{\mathcal{V}}, \hat{\mathbf{z}}^{\mathcal{V}}$ where $\hat{\mathbf{z}}^{\mathcal{V}} = \hat{\mathbf{x}}^{\mathcal{V}} \times \hat{\mathbf{y}}^{\mathcal{V}}$ is aligned with the camera boresight. The VBS may be pointed as necessary to keep targets in the field of view (FOV). Figure 2 provides an example.

2.3 System State

The absolute orbit α of an observer can be parametrized by quasi-nonsingular orbit elements (OE), with

$$\begin{aligned} \alpha &= [a \ e_x \ e_y \ i \ \Omega \ u]^\top \\ &= [a \ e \cos \omega \ e \sin \omega \ i \ \Omega \ \omega + M]^\top \end{aligned} \quad [1]$$

Above, a, e, i, Ω, ω , and M are the canonical Keplerian OE of semi-major axis, eccentricity, inclination, right ascension of the ascending node, argument of periaapsis, and mean anomaly respectively, and u is

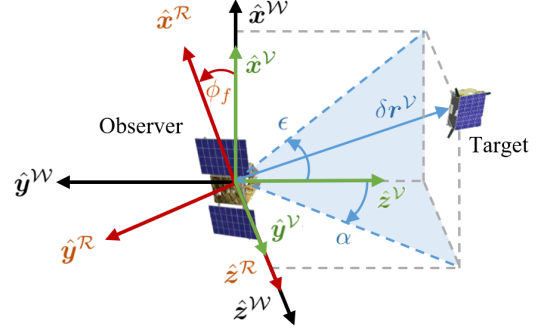


Fig. 2: Definition of \mathcal{V}, \mathcal{R} and \mathcal{W} with the VBS pointing in the anti-velocity direction. Bearing angles $[\alpha, \epsilon]$ are shown for target line-of-sight vector $\delta r^{\mathcal{V}}$.

the mean argument of latitude. All are defined with respect to \mathcal{I} . Fully nonsingular OE [17] can be used for equatorial orbits. Absolute orbits can be equivalently expressed in Cartesian form $\mathbf{x}^{\mathcal{I}}$ with components

$$\mathbf{x}^{\mathcal{I}} = \begin{bmatrix} \mathbf{r}^{\mathcal{I}} \\ \mathbf{v}^{\mathcal{I}} \end{bmatrix} = [r_x, r_y, r_z, v_x, v_y, v_z]^\top \quad [2]$$

where \mathbf{r} is position and \mathbf{v} is velocity.

Relative orbits $\delta\alpha$ of targets with respect to an observer can be parametrized by quasi-nonsingular relative orbit elements (ROE) [18]. The ROE are defined in terms of the OE of the observer and target (denoted by subscripts 'o' and 't' respectively) via

$$\begin{aligned} \delta\alpha &= [\delta a \ \delta\lambda \ \delta e_x \ \delta e_y \ \delta i_x \ \delta i_y]^\top \\ &= \begin{pmatrix} \delta a \\ \delta\lambda \\ |\delta e| \cos \phi \\ |\delta e| \sin \phi \\ |\delta i| \cos \theta \\ |\delta i| \sin \theta \end{pmatrix} = \begin{pmatrix} (a_t - a_o)/a_o \\ (u_t - u_o) + (\Omega_t - \Omega_o) \cos i_o \\ e_{x,t} - e_{x,o} \\ e_{y,t} - e_{y,o} \\ i_t - i_o \\ (\Omega_t - \Omega_o) \sin i_o \end{pmatrix} \end{aligned} \quad [3]$$

Above, δa is the relative semi-major axis, $\delta\lambda$ is the relative mean longitude, $\delta e = (\delta e_x, \delta e_y)$ is the relative eccentricity vector with magnitude δe and phase ϕ , and $\delta i = (\delta i_x, \delta i_y)$ is the relative inclination vector with magnitude δi and phase θ . Fully nonsingular ROE have been defined for equatorial orbits [19].

Estimation of auxiliary state components can provide additional robustness and autonomy. States may include the absolute clock offset and drift rate of an observer, \mathbf{c}_{err} , and its differential clock parameters with respect to other observers, $\delta\mathbf{c}_{\text{err}}$, denoted as

$$\mathbf{c}_{\text{err}} = \begin{pmatrix} c_{\text{err}} \\ d_{\text{err}} \end{pmatrix} \quad \delta\mathbf{c}_{\text{err}} = \begin{pmatrix} \delta c_{\text{err}} \\ \delta d_{\text{err}} \end{pmatrix} = \mathbf{c}_{\text{err},t} - \mathbf{c}_{\text{err},o} \quad [4]$$

2.4 Measurement Model

Above, c_{err} is a clock offset and d_{err} is a drift rate. The absolute ballistic coefficients of an object, \mathbf{B} , and differential ballistic coefficients of its targets, $\delta\mathbf{B}$, can also be estimated, denoted as

$$\mathbf{B} = \begin{pmatrix} B_{\text{atm}} \\ B_{\text{srp}} \end{pmatrix} \quad \delta\mathbf{B} = \begin{pmatrix} \delta B_{\text{atm}} \\ \delta B_{\text{srp}} \end{pmatrix} = \mathbf{B}_t - \mathbf{B}_o \quad [5]$$

where subscripts ‘atm’ and ‘srp’ refer to atmospheric drag and solar radiation pressure (SRP) respectively. Finally, VBS measurement biases of observers can be estimated, denoted as $\mathbf{b} = [b_\alpha, b_\epsilon]^T$.

Consider a system of N_o active observers and N_p passive objects. The system absolute orbit state is

$$\mathbf{x}_\alpha = [\alpha_1, \alpha_2, \dots, \alpha_{N_o+N_p}] \quad [6]$$

The system absolute auxiliary state vector is

$$\mathbf{x}_{\text{aux}} = [c_1, \dots, c_{N_o}, \mathbf{B}_1, \dots, \mathbf{B}_{N_o+N_p}, \mathbf{b}_1, \dots, \mathbf{b}_{N_o}] \quad [7]$$

Consider the subsystem of an observer i which contains N_c^i cooperative remote observers and N_p^i passive target objects. The subsystem orbit state vector is

$$\mathbf{x}_\alpha = [\alpha_i, \delta\alpha_1, \delta\alpha_2, \dots, \delta\alpha_{N_c^i+N_p^i}] \quad [8]$$

The subsystem auxiliary state vector is

$$\mathbf{x}_{\text{aux}} = [c_i, \delta c_1, \delta c_2, \dots, \delta c_{N_c^i}, \mathbf{B}_i, \delta\mathbf{B}_1, \delta\mathbf{B}_2, \dots, \delta\mathbf{B}_{N_c^i+N_p^i}, \mathbf{b}_1, \mathbf{b}_2, \dots, \mathbf{b}_{N_c^i+1}] \quad [9]$$

2.4 Measurement Model

Bearing angles consist of azimuth and elevation $[\alpha, \epsilon]$ and subtend the line-of-sight vector $\delta\mathbf{r}^\mathcal{V}$ from the observer to the target. The measurement model \mathbf{y} for the bearing angles from spacecraft i to spacecraft j is described by [3]

$$\delta\mathbf{r}_{ji}^\mathcal{V} = \mathbf{r}_j^\mathcal{V} - \mathbf{r}_i^\mathcal{V} = [\delta r_x^\mathcal{V}, \delta r_y^\mathcal{V}, \delta r_z^\mathcal{V}]^\top \quad [10]$$

$$\mathbf{y}_{ji}^\mathcal{V}(\mathbf{x}) = \begin{bmatrix} \alpha \\ \epsilon \end{bmatrix}^\mathcal{V} = \begin{bmatrix} \arcsin \delta r_y^\mathcal{V} / \|\delta\mathbf{r}_{ji}^\mathcal{V}\|_2 \\ \arctan \delta r_x^\mathcal{V} / \delta r_z^\mathcal{V} \end{bmatrix} \quad [11]$$

Figure 2 depicts the measurement model. Bearing angles are related to the inertial frame by rotating $\delta\mathbf{r}^\mathcal{V}$ into \mathcal{I} , as per $\delta\mathbf{r}^\mathcal{I} = {}^\mathcal{V}\tilde{\mathbf{R}}^\mathcal{I} \delta\mathbf{r}^\mathcal{V}$ where ${}^\mathcal{V}\tilde{\mathbf{R}}^\mathcal{I}$ denotes a rotation from frame \mathcal{V} into frame \mathcal{I} . This rotation is generally computed by performing attitude determination using stars identified by the VBS [8]. Other relevant rotations ${}^\mathcal{R}\tilde{\mathbf{R}}^\mathcal{I}$ and ${}^\mathcal{W}\tilde{\mathbf{R}}^\mathcal{I}$ can be computed using the observer’s absolute orbit estimate.

There is an equivalence between bearing angles and the measured unit vector from observer to target [13]. The measurement model \mathbf{z} for the inertial unit vector from spacecraft i to spacecraft j is

$$\mathbf{z}_{ji}^\mathcal{I}(\mathbf{x}) = \frac{\delta\mathbf{r}_j^\mathcal{I} - \mathbf{r}_i^\mathcal{I}}{\|\mathbf{r}_j^\mathcal{I} - \mathbf{r}_i^\mathcal{I}\|_2} = \frac{\delta\mathbf{r}_{ji}^\mathcal{I}}{\delta r_{ji}^\mathcal{I}} \quad [12]$$

In practice, the model is affected by optical visibility including eclipse periods, sun-blinding of the camera, visual magnitude of the target, and limited camera FOV. When required, visual magnitudes are computed using a model [20] that accounts for surface properties, solar phase angle and albedo.

Spacecraft may also be able to obtain absolute position and velocity information via GNSS, the DSN, or inter-satellite sharing of state estimates. In \mathcal{I} , the measurement of the absolute state of spacecraft i is

$$\mathbf{z}_i^\mathcal{I}(\mathbf{x}) = \begin{bmatrix} \mathbf{r}_i^\mathcal{I} \\ \mathbf{v}_i^\mathcal{I} \end{bmatrix} \quad [13]$$

2.5 Dynamics Model

The dynamics model for each object’s Cartesian state, using Keplerian dynamics, is [17]

$$\dot{\mathbf{x}}_i = \mathbf{f}(\mathbf{x}) = \begin{bmatrix} \dot{\mathbf{r}}_i^\mathcal{I} \\ \dot{\mathbf{v}}_i^\mathcal{I} \end{bmatrix} = \begin{bmatrix} \mathbf{v}_i^\mathcal{I} \\ -\mu\mathbf{r}_i^\mathcal{I} / \|\mathbf{r}_i^\mathcal{I}\|_3^3 \end{bmatrix} \quad [14]$$

for gravitational parameter μ of the central body. Orbits are also affected by perturbing forces including spherical harmonic gravity, atmospheric drag, third-body gravity and SRP. To include these effects, the osculating OE of each spacecraft can be propagated using numerical integration of the Gauss Variational Equations (GVE). For orbit state α , the osculating OE of each spacecraft evolve according to $\dot{\alpha} = G(\alpha)\mathbf{d}^\mathcal{R}$ where $G \in \mathbf{R}^{6 \times 3}$ is the well-documented GVE matrix [21] and $\mathbf{d}^\mathcal{R}$ is the perturbing acceleration expressed in \mathcal{R} . Maneuvers also affect spacecraft orbits and typically improve observability if maneuver parameters are known to the observer [14]. This research assumes maneuvers are not performed. Analytic models for mean OE and ROE which include effects of J_2 , SRP, differential drag and other perturbations have also been developed and can be applied when computational efficiency is paramount [19, 22, 23].

Spacecraft clock states evolve according to a discrete time random walk process [24] defined by

$$\mathbf{c}_{t_k} = \Phi_c \mathbf{c}_{t_{k-1}} + \mathcal{N}(\mathbf{0}, \Sigma_c) \quad [15]$$

$$\Phi_c = \begin{bmatrix} 1 & T_s \\ 0 & 1 \end{bmatrix} \quad \Sigma_c = \begin{bmatrix} q_1 T_s + q_2 \frac{T_s^3}{3} & q_2 \frac{T_s^2}{2} \\ q_2 \frac{T_s^2}{2} & q_2 T_s \end{bmatrix}$$

3. Analytic Observability

Above, T_s is the propagation timestep between epochs t_k and t_{k-1} ; \mathcal{N} is a normal distribution with zero mean and the stated covariance; and q_1 and q_2 are clock-specific constants. In this paper, ballistic coefficients and sensor biases are modeled as constants.

3. Analytic Observability

Graph-based observability analysis links the observability of a distributed system to a graph representing the flow of measurement information between its members [25]. Here, graph topologies are combined with prior Lie derivative results to propose sufficient graphical conditions for system orbit observability, providing a simple initial indication of whether orbits are likely to be strongly or weakly observable in the analytic sense. Prior research has assumed instantaneous global information access across the system [12, 13] whereas this work assumes observers have limited access to measurement information. This allows more granular modeling of observability variations for different observers and inclusion of physical system limitations.

3.1 Topology Definition

Consider a system of N_s objects forming the set \mathcal{S} . Within \mathcal{S} are subsets of observers \mathcal{O} , passive objects \mathcal{P} , and beacons \mathcal{B} . Beacons may be either external beacons $\mathcal{B}_e \subseteq \mathcal{B}$ or internal beacons $\mathcal{B}_i \subseteq \mathcal{B}$. The system directed measurement graph [26] is defined as $\mathcal{G} = \{\mathcal{S}, \mathcal{M}, \mathcal{W}\}$. $\mathcal{S} = \mathcal{O} \cup \mathcal{P} \cup \mathcal{B}$ is the set of graph nodes and object states to be estimated. $\mathcal{M} \subseteq \mathcal{S} \times \mathcal{S}$ is the set graph edges. Edges describes the directed flow of measurement information from target to observer. \mathcal{W} is the weight corresponding to each edge. An edge from target j to observer i is denoted $j \rightarrow i$ with weight w_{ji} . Edges may represent absolute position measurements (iff $j \in \mathcal{B}$) or bearing angles. Unless specified, $w_{ji} = 1$. Figure 3 presents an example. Observers may also communicate over the ISL: consider a set \mathcal{C} of directed communication edges which allow sharing of relevant measurement information. Figure 4 presents an example with $\mathcal{C} = \{a \rightarrow c, c \rightarrow d, d \rightarrow c\}$. The resulting measurement edges are displayed in Figure 5.

Define \mathcal{T}_i as the set of targets of observer i and \mathcal{C}_i as the set of remote observers i communicates with. Then i receives measurements of (and estimates the states of) objects in subsystem $\mathcal{S}_i = \mathcal{T}_i \cup \mathcal{C}_i \cup \{i\}$. Denote the complete set of targets for all $j \in \mathcal{C}_i$ as $\mathcal{T}_{\mathcal{C}_i} = \{k \mid k \in \mathcal{T}_j, j \in \mathcal{C}_i\}$. As per Section 2, observer i only utilizes measurements of targets $k \in \mathcal{S}_i$. There-

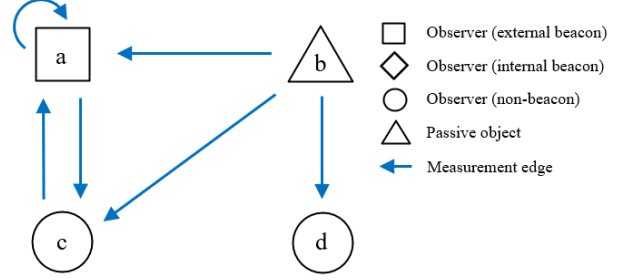


Fig. 3: Here, a measures b and c ; c measures a and b ; and d measures b

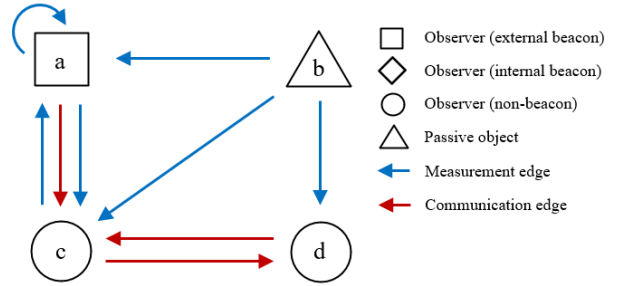


Fig. 4: Here, a sends messages to c while c and d exchange messages.

fore \mathcal{M}_i , or the set of measurement edges directed to i , is the union of six subsets:

1. If $i \in \mathcal{B}_e$: An absolute orbit measurement of i .
2. If $\{\mathcal{C}_i \cap \mathcal{B}\} \neq \emptyset$: Remote absolute orbit measurements of beacons in \mathcal{C}_i .
3. If $i \in \mathcal{T}_{\mathcal{C}_i}$: Remote bearing angles of i .
4. If $\mathcal{T}_i \neq \emptyset$: Local bearing angles of targets in \mathcal{T}_i .
5. If $\{\mathcal{T}_{\mathcal{C}_i} \cap \mathcal{T}_i\} \neq \emptyset$: Remote bearing angles of targets in \mathcal{T}_i .
6. If $\{\mathcal{T}_{\mathcal{C}_i} \cap (\mathcal{C}_i \setminus \mathcal{T}_i)\} \neq \emptyset$: Remote bearing angles of observers in \mathcal{C}_i not already targets in \mathcal{T}_i .

\mathcal{M}_i is enumerated as

$$\begin{aligned} \mathcal{M}_i = & \{(i \in \mathcal{B}_e) \rightarrow i\} \cup \{(\mathcal{C}_i \cap \mathcal{B}) \rightarrow i\} \cup \\ & \{\{j \mid i \in \mathcal{T}_j, j \in \mathcal{C}_i\} \rightarrow i\} \cup \{\mathcal{T}_i \rightarrow i\} \cup \\ & \{(\mathcal{T}_i \cap \mathcal{T}_{\mathcal{C}_i}) \rightarrow i\} \cup \{[\mathcal{T}_{\mathcal{C}_i} \cap (\mathcal{C}_i \setminus \mathcal{T}_i)] \rightarrow i\} \end{aligned} \quad [16]$$

and the complete set of graph edges is $\mathcal{M} = \cup_{i \in \mathcal{O}} \mathcal{M}_i$. This definition explicitly accounts for distribution and limited communication and furthermore, observability of individual subsystems can be examined and designed via subgraphs $\mathcal{G}_i = \{\mathcal{S}_i, \mathcal{M}_i, \mathcal{W}_i\}$. Subsequent sections discuss computation of weights \mathcal{W} and consolidation of multiple identical edges into a single

3.2 Topology Generation

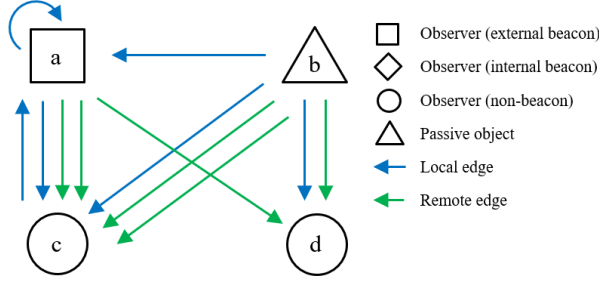


Fig. 5: Here, local edges correspond to measurement edges from Fig. 3 and remote edges are created by communication edges in Fig. 4. Object c receives measurements of b from a and d ; and measurements of itself and a from a . Object d receives measurements of a and b from c .

edge with increased weight.

3.2 Topology Generation

By defining $\mathcal{B}, \mathcal{O}, \mathcal{P}$, graph nodes \mathcal{S} can be enumerated. By defining \mathcal{T}_i and \mathcal{C}_i for all $i \in \mathcal{S}$, graph edges \mathcal{M} can be enumerated. It is proposed to generate physically realistic \mathcal{T}_i and \mathcal{C}_i by simulation of DSS states and measurements. Necessary simulation parameters include the dynamics model; number of spacecraft, their roles, and initial OE; sensor attitude, FOV, and detectable magnitude; radio communication range; measurement frequency and collection period. Via numerical integration of the GVE, the orbits of all system objects can be simulated and bearing angles throughout the simulation period can be computed. Bearing angles are valid if they lie within the sensor FOV, are below the maximum detectable magnitude, are not affected by eclipses or sun blinding, and the remote observer (if applicable) is within ISL range. If there is a sufficient number of valid measurements N_m^{ji} between observer i and target j such that $N_m^{ji} \geq N_m^{\min}$, then $\mathcal{T}_i = \mathcal{T}_i \cup j$. If there is a sufficient period of communication N_c^{ki} between i and a remote observer k with $\{\{i \cup \mathcal{T}_i\} \cap \mathcal{T}_k\} \neq \emptyset$ and $N_c^{ki} \geq N_c^{\min}$, then $\mathcal{C}_i = \mathcal{C}_i \cup k$. Constants N_m^{\min}, N_c^{\min} are user-defined. Physical system constraints are thus explicitly accounted for.

3.3 Lie Derivative Analysis

Graph observability can be analytically assessed by applying Lie derivative results. Consider a system of N_s objects whose states are to be estimated using N_m unit vector measurements. The system model

expressed in state space form is

$$\dot{\mathbf{x}} = \mathbf{f}(\mathbf{x}) = \begin{bmatrix} \mathbf{f}(\mathbf{x}_1) \\ \mathbf{f}(\mathbf{x}_2) \\ \vdots \\ \mathbf{f}(\mathbf{x}_{N_s}) \end{bmatrix} \quad \mathbf{z} = \mathbf{h}(\mathbf{x}) = \begin{bmatrix} \mathbf{z}_1(\mathbf{x}) \\ \mathbf{z}_2(\mathbf{x}) \\ \vdots \\ \mathbf{z}_{N_m}(\mathbf{x}) \end{bmatrix} \quad [17]$$

where $\mathbf{x} \in \mathbb{R}^{6N_s}$ and $\mathbf{z} \in \mathbb{R}^{3N_m}$. The zeroth- and first-order Lie-derivatives of the system are

$$L_f^0 \mathbf{h}(\mathbf{x}) = \mathbf{h}(\mathbf{x}) \quad L_f^1 \mathbf{h}(\mathbf{x}) = \frac{\partial \mathbf{h}(\mathbf{x})}{\partial \mathbf{x}} \mathbf{f}(\mathbf{x}) \quad [18]$$

and the q -order Lie-derivative is

$$L_f^q \mathbf{h}(\mathbf{x}) = L_f(L_f^{q-1} \mathbf{h}(\mathbf{x})) \quad [19]$$

The observability matrix \mathbf{O} for the system is then

$$\mathbf{O}_q = \frac{\partial}{\partial \mathbf{x}} \begin{bmatrix} L_f^0 \mathbf{h}(\mathbf{x}) \\ L_f^1 \mathbf{h}(\mathbf{x}) \\ L_f^2 \mathbf{h}(\mathbf{x}) \\ \vdots \\ L_f^q \mathbf{h}(\mathbf{x}) \end{bmatrix} = \frac{\partial}{\partial \mathbf{x}} \begin{bmatrix} \mathbf{h}(\mathbf{x}) \\ \frac{\partial \mathbf{h}(\mathbf{x})}{\partial \mathbf{x}} \mathbf{f}(\mathbf{x}) \\ \frac{\partial^2 \mathbf{h}(\mathbf{x})}{\partial \mathbf{x}^2} \mathbf{f}(\mathbf{x})^2 \\ \vdots \\ \frac{\partial^q \mathbf{h}(\mathbf{x})}{\partial \mathbf{x}^q} \mathbf{f}(\mathbf{x})^q \end{bmatrix} \quad [20]$$

The Lie derivative criterion states that if $\text{rank}(\mathbf{O}_q) = 6N_s$ for some $q > 0$ and there are $6N_s$ linearly independent columns of \mathbf{O}_q , the system is locally weakly observable (LWO) at \mathbf{x} to q^{th} -order [27]. Note that intuitively, rows of \mathbf{O}_q correspond to measurement information and columns of \mathbf{O}_q correspond to the state space to be estimated. Thus, the aim of the criterion is to show that enough measurement information exists to observe or ‘span’ the estimated state. Angles-only space systems have been investigated to 2nd- and 3rd-order by Hu et al. [12, 13] using Keplerian dynamics, Cartesian states and unit vector measurements. It is proven that a system composed of an external beacon and N_t targets is second-order LWO if at least N_t edges fully connect all targets and the beacon. Furthermore, a system without a beacon consisting of N_s objects is third-order LWO if at least N_s edges fully connect all objects. In other words, the observer must have access to $N_m \geq N_s$ unique measurements, where ‘unique’ measurements occur between a unique object pair. Hu et al. also show that for some \mathbf{z}_{ij} to contribute to observability, i and j must possess distinct orbit planes or distinct orbit altitudes. In ROE, this corresponds to $\delta i \neq 0$ (distinct orbit planes) and $e \neq \delta e \neq 0$ or $\delta a \neq 0$ (distinct orbit altitudes). Measurements fulfilling this condition are ‘proper’ as opposed to ‘improper’. In practice, perturbed dynamics improve observability and make improper edges somewhat observable, but graphs with proper edges remain comparatively much more observable, as demonstrated in Section 4.

3.4 Observability Conditions

3.4 Observability Conditions

Table 1 summarizes observability when the criteria of [12] are applied to measurement sets for two- and three-spacecraft subsystems. Rows 2 and 5 of Table 1 are unobservable because $N_m < N_s$. In Row 3 of Table 1, even though $N_m \geq N_s$, the system is unobservable. Equation 11 implies $\mathbf{z}_{ji} = -\mathbf{z}_{ij}$ such that the measurements are non-unique; the \mathbf{z}_{ij} rows of \mathbf{O}_q are a linear combination of existing \mathbf{z}_{ji} rows and cannot increase matrix rank. Remaining rows of Table 1 are observable because either $N_m \geq N_t$ for systems with beacons (Rows 1, 4) or $N_m \geq N_s$ for systems without beacons (Rows 6, 7) with all measurements occurring between unique object pairs.

In summary, consider an observer with a two- or three-spacecraft subsystem. If the observer is an internal beacon, its own orbit is observable by definition. For an observer to be an internal beacon, as per Table 1, it requires access to one or more of the following sets of subsystem information:

1. A remote bearing angle of itself, measured by
 - (a) Another observer which is a beacon (Row 1 in Table 1)
 - (b) Another observer, which is itself a target of the local observer (Row 7 in Table 1)
2. A local bearing angle of a target, and a remote bearing angle of the same target, measured by
 - (a) Another local target (Row 6 in Table 1)
 - (b) Another observer which is a beacon (Row 4 in Table 1)

Now consider an observer with a subsystem of arbitrary size. If at least one two- or three-spacecraft subgraph of its nodes and edges fulfils the above conditions, it likewise becomes an internal beacon. Via the Lie derivative conditions, the orbits of any targets connected to it via measurement edges are also observable. Complete system observability is achieved when each observer is a beacon or the target of a beacon, and each passive object is the target of a beacon. Measurements granting observability must additionally be proper. These conditions are considered sufficient for angles-only observability, as is demonstrated in Section 4. Systems fulfilling the above conditions are ‘proper’; systems which do not are ‘improper’. To formally apply these conditions to the earlier topology condition, Algorithm 1 is proposed for determining analytic observability. The following paragraphs describe its reasoning with an accompanying example in Figure 6.

Step 1) in Algorithm 1 initializes graph nodes, as

| Objects | States | Meas. List | Observability |
|---------------------|----------------|--|-----------------------------|
| $i \in \mathcal{B}$ | \mathbf{x}_i | \mathbf{z}_i | 2 nd -order |
| $j \in \mathcal{P}$ | \mathbf{x}_j | \mathbf{z}_{ji} | |
| $i \in \mathcal{O}$ | \mathbf{x}_i | \mathbf{z}_{ji} | None |
| $j \in \mathcal{P}$ | \mathbf{x}_j | | (to 3 rd -order) |
| $i \in \mathcal{O}$ | \mathbf{x}_i | \mathbf{z}_{ji} | None |
| $j \in \mathcal{O}$ | \mathbf{x}_j | $\mathbf{z}_{ij} (= -\mathbf{z}_{ji})$ | (to 3 rd -order) |
| $i \in \mathcal{B}$ | \mathbf{x}_i | \mathbf{z}_i | 2 nd -order |
| $j \in \mathcal{O}$ | \mathbf{x}_j | \mathbf{z}_{ki} | |
| $k \in \mathcal{P}$ | \mathbf{x}_k | \mathbf{z}_{kj} | |
| $i \in \mathcal{O}$ | \mathbf{x}_i | \mathbf{z}_{ki} | None |
| $j \in \mathcal{O}$ | \mathbf{x}_j | \mathbf{z}_{kj} | (to 3 rd -order) |
| $k \in \mathcal{P}$ | \mathbf{x}_k | | |
| $i \in \mathcal{O}$ | \mathbf{x}_i | \mathbf{z}_{ki} | 3 rd -order |
| $j \in \mathcal{O}$ | \mathbf{x}_j | \mathbf{z}_{kj} | |
| $k \in \mathcal{P}$ | \mathbf{x}_k | \mathbf{z}_{ji} | |
| $i \in \mathcal{O}$ | \mathbf{x}_i | \mathbf{z}_{ki} | 3 rd -order |
| $j \in \mathcal{O}$ | \mathbf{x}_j | \mathbf{z}_{ij} | |
| $k \in \mathcal{O}$ | \mathbf{x}_k | \mathbf{z}_{jk} | |

Table 1: Analytic observability results when applying measurement conditions from [12].

defined by the user. Step 2) generates visible local targets and connected remote observers for each observer, either pre-defined by the user or computed through simulation. Step 3) initializes graph edges and edge weights.

Step 4) initializes graph edges for each observer subsystem. If the subsystem contains N_s objects, including the observer, there may be $N_s - 1$ edges specifically directed to the observer. Additionally, if the observer is an external beacon, there is an edge directed from itself to itself. Edges from local targets to the observer are initialized with $w = 1$ because these measurements are available by definition. Edges from remote observers (which are not local targets) to the observer are initialized with $w = 0$ because these measurements are not necessarily available.

Step 5) accounts for remote measurements. If the remote observer is a beacon, it broadcasts its known orbit state by definition and the corresponding w is incremented. Similarly, if the observer receives a remote measurement of a local target, the edge is geometrically unique and the corresponding w is incremented. In this fashion, edge weights explicitly count the number of distinct measurements of an object. If the observer receives a remote measurement of itself, recall that the measurement is not distinct if the remote observer is also a local target; thus, w is only incremented if this is not the case.

3.4 Observability Conditions

Algorithm 1: Compute system topology and analytic observability.

Data: System parameters.

Result: System topology and analytic observability.

1. Initialize $\mathcal{B}, \mathcal{O}, \mathcal{P}, \mathcal{S}$ from inputs.
 2. For all $i \in \mathcal{O}$:
 - (a) Generate $\mathcal{T}_i, \mathcal{C}_i$ from inputs.
 - (b) For all $j \in \mathcal{C}_i$: add $j \rightarrow i$ to \mathcal{C} .
 3. Initialize $\mathcal{M} = \mathcal{W} = \emptyset$.
 4. For all $i \in \mathcal{O}$:
 - (a) If $i \in \mathcal{B}_e$: add $i \rightarrow i$ to \mathcal{M} ; $w_{ii} = 1$ to \mathcal{W} .
 - (b) For all $j \in \mathcal{T}_i$: add $j \rightarrow i$ to \mathcal{M} ; $w_{ji} = 1$ to \mathcal{W} .
 - (c) For all $j \in (\mathcal{C}_i \setminus \mathcal{T}_i)$: add $j \rightarrow i$ to \mathcal{M} ; $w_{ji} = 0$ to \mathcal{W} .
 5. For all $j \rightarrow i$ in \mathcal{C} :
 - (a) If $j \in \mathcal{B}$: $w_{ji} += 1$.
 - (b) For all targets $k \in \mathcal{T}_j$:
 - If $k \in (\mathcal{T}_i \cup \mathcal{C}_i)$: $w_{ki} += 1$.
 - If $(k = i) \wedge (j \notin \mathcal{T}_i)$: $w_{ji} += 1$.
 6. For all $i \in (\mathcal{O} \setminus \mathcal{B})$:
 - If $(\sum_{j \in \mathcal{S}_i} w_{ji}) \geq \text{card}(\mathcal{S}_i)$: add i to \mathcal{B}_i .
 7. Repeat Steps 3-6 until \mathcal{B}_i is unchanged between iterations.
 8. For all $i \in \mathcal{O}$:
 - If $i \notin \mathcal{B}$: i is cannot observe the orbit state of its subsystem. Modifications are required.
 9. For all $i \in \mathcal{P}$:
 - If $\{j \rightarrow i \mid j \in \mathcal{B}\} \cap \mathcal{M} = \emptyset$: the orbit of i is unobservable. Modifications are required.
-

Step 6) examines observability of each observer's subsystem. To estimate its own orbit, it has been established that the observer requires $N_m \geq N_s$. Thus, if the sum of edge weights is greater than or equal to the number of objects in the subsystem, the observer's orbit is the observable and it becomes a beacon. Consequently, orbits of all objects connected to it via directed measurement edges are observable.

Step 7) notes that observers may be promoted to internal beacons if they meet topological conditions. If so, connectivity is improved: in addition to bearing angles, beacons broadcast an absolute orbit estimate and subsequently increase edge weights as per Step 5a). Thus, if observer i becomes a beacon, other observers j with $i \in \mathcal{C}_j$ may also promote to beacons. Propagation of beacon status throughout the system is accounted for by repeating Steps 3) to 6). Step 8) confirms that each observer is a beacon that may observe the orbit state of its subsystems. Step 9)

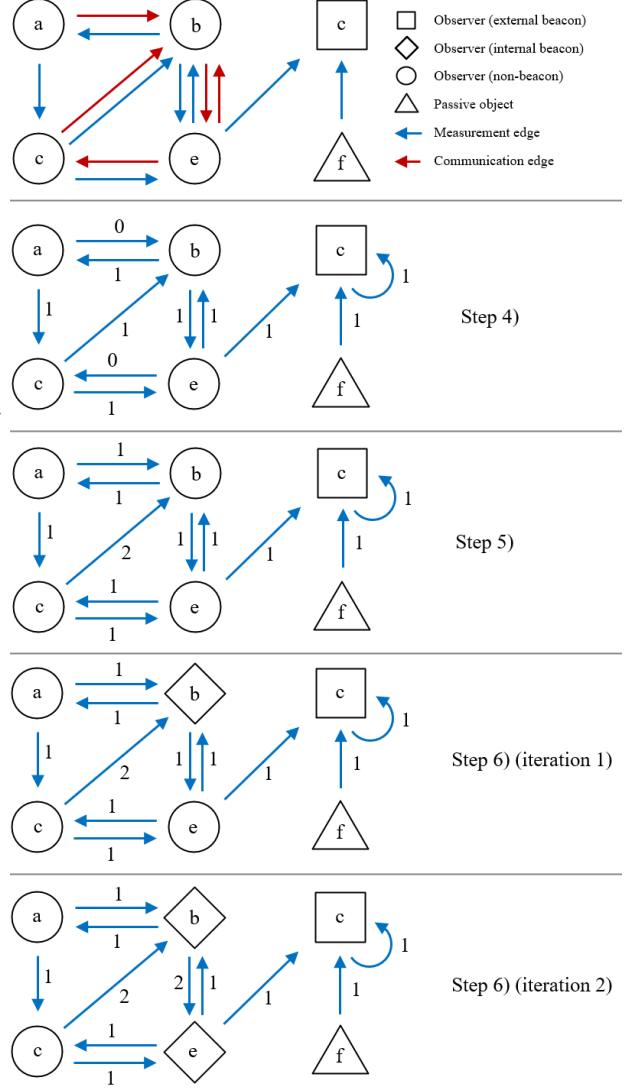


Fig. 6: An example progression of Algorithm 1 for a six-object system.

confirms that all passive objects are the target of a beacon are thus observable.

Inclusion of graph weights allows for a simple per-subsystem visual assessment of observability as well as a basic assessment of quality of observability: the greater the ratio

$$q_i = \left(\sum_{j \in \mathcal{S}_i} w_{ji} \right) / \text{card}(\mathcal{S}_i) \quad [21]$$

the more unique measurements are available to the observer with correspondingly stronger observability (ignoring other factors such as measurement quality).

4. Numeric Observability

Numeric observability analysis quantitatively characterizes system state observability for a given set of input measurements. In contrast to the analytic approach, the numeric approach incorporates system-level errors and uncertainties, perturbed dynamics, and auxiliary state observability. It therefore provides a more rigorous and physically relevant result at the cost of additional computation. This research extends the method of Koenig et al. [4, 10, 11] which directly estimates a state covariance matrix using measurement sensitivity and noise matrices. This is preferred over other metrics such as the observability Gramian because estimated uncertainty of specific state components can be directly related to mission requirements. Specific extensions include the effects of dynamics model uncertainty, partial measurement availability, and added auxiliary states.

4.1 Covariance Formulation

Consider a function providing a set of local measurements \mathbf{m} to an observer, as a function of observer index i , state estimation epoch t_0 , system state $\mathbf{x}_0 = \mathbf{x}(t_0)$, and measurement epoch t . Recall the clock offset of observer i at epoch t , $c_{\text{err}}(i, t_0, \mathbf{x}_0, t)$. Then, the function has the form

$$\mathbf{m}_i(t) = \mathbf{h}(i, t_0, \mathbf{x}_0, t + c_{\text{err}}(i, t_0, \mathbf{x}_0, t)) \quad [22]$$

Measurements are computed by propagating \mathbf{x}_0 from t_0 to measurement epoch t and applying the relevant measurement model to the propagated state.

Let there be remote observers $\mathcal{C}_i = \{j, k, l, \dots\}$ such that the set of subsystem observers is $\mathcal{O}_i = \{i, j, k, l, \dots\}$. The batch of measurements received by observer i from itself and connected remote observers at epoch t is $\mathbf{M}_i(t)$. Furthermore, let measurements be provided at N_t epochs t_1, \dots, t_{N_t} , collectively referred to as \mathbf{t}_m . Across all epochs, the batch of measurements received by observer i is $\mathbf{M}_i(\mathbf{t}_m)$, with

$$\mathbf{M}_i(t) = \begin{pmatrix} \mathbf{m}_i(t) \\ \mathbf{m}_j(t) \\ \mathbf{m}_k(t) \\ \vdots \end{pmatrix} \quad \mathbf{M}_i(\mathbf{t}_m) = \begin{pmatrix} \mathbf{M}_i(t_1) \\ \vdots \\ \mathbf{M}_i(t_{N_t}) \end{pmatrix} \quad [23]$$

Partition state \mathbf{x} into estimated components \mathbf{x}_{est} and components provided a-priori $\mathbf{x}_{\text{prior}}$. The sensitivity matrix \mathbf{Y}_{est} is formed by evaluating the partial derivatives of each measurement with respect to each component of \mathbf{x}_{est} , via

$$\mathbf{Y}_{\text{est}} = \frac{\partial \mathbf{M}_i(\mathbf{t}_m)}{\partial \mathbf{x}_{\text{est}}} \Big|_{\mathbf{x}} \quad [24]$$

Partial derivatives are computed using central differences with

$$\mathbf{h}^{\pm} = \mathbf{h}(i, t_0, \mathbf{x}_0 \pm \Delta \mathbf{x}, t + c_{\text{err}}(i, t_0, \mathbf{x}_0 \pm \Delta \mathbf{x}, t))$$

$$\frac{\partial \mathbf{h}}{\partial \mathbf{x}} \Big|_{\mathbf{x}} = \frac{\mathbf{h}^+ - \mathbf{h}^-}{2 \|\Delta \mathbf{x}\|} \quad [25]$$

where $\Delta \mathbf{x}$ is a vector that is zero except for the state component where sensitivity is being evaluated.

The observability analysis leverages the following model [11] for the relationship between covariance matrix \mathbf{R} for the measurement batch and covariance matrix \mathbf{P}_{est} for the estimated state, given by

$$\mathbf{R} = \mathbf{Y}_{\text{est}} \mathbf{P}_{\text{est}} \mathbf{Y}_{\text{est}}^{\top} \quad [26]$$

When \mathbf{Y}_{est} is full column rank, \mathbf{P}_{est} is computed as

$$\mathbf{P}_{\text{est}} = \left(\mathbf{Y}_{\text{est}}^{\top} \mathbf{Y}_{\text{est}} \right)^{-1} \left(\mathbf{Y}_{\text{est}}^{\top} \mathbf{R} \mathbf{Y}_{\text{est}} \right) \left(\mathbf{Y}_{\text{est}}^{\top} \mathbf{Y}_{\text{est}} \right)^{-1} \quad [27]$$

The matrix \mathbf{R} consists of three covariance contributions, with

$$\mathbf{R} = \mathbf{R}_{\text{sen}} + \mathbf{R}_{\text{prior}} + \mathbf{R}_{\text{dyn}} \quad [28]$$

\mathbf{R}_{sen} denotes measurement noise arising from the sensor, $\mathbf{R}_{\text{prior}}$ denotes measurement noise arising from uncertainty in any a-priori information, and \mathbf{R}_{dyn} denotes measurement noise arising from dynamics model uncertainty (e.g. due to unmodeled or mismodeled perturbations). \mathbf{R}_{sen} and $\mathbf{R}_{\text{prior}}$ are given by

$$\mathbf{R}_{\text{sen}} = \begin{bmatrix} \mathbf{R}_{\text{meas}} & \mathbf{0} & \dots & \mathbf{0} \\ \mathbf{0} & \mathbf{R}_{\text{meas}} & \dots & \mathbf{0} \\ \vdots & \vdots & \ddots & \vdots \\ \mathbf{0} & \mathbf{0} & \dots & \mathbf{R}_{\text{neas}} \end{bmatrix} \quad [29]$$

$$\mathbf{R}_{\text{prior}} = \mathbf{Y}_{\text{prior}} \mathbf{P}_{\text{prior}} \mathbf{Y}_{\text{prior}}^{\top} \quad [30]$$

where \mathbf{R}_{meas} is the measurement noise covariance for a single measurement. Independent measurements with identical noise distributions are assumed. A typical choice for bearing angles is $\mathbf{R}_{\text{meas}} = (20'')^2 \mathbf{I}_2$. The new \mathbf{R}_{dyn} term is given by

$$\mathbf{R}_{\text{dyn}} = \begin{bmatrix} \mathbf{R}_{\text{proc}} & \mathbf{0} & \dots & \mathbf{0} \\ \mathbf{0} & \mathbf{R}_{\text{proc}} & \dots & \mathbf{0} \\ \vdots & \vdots & \ddots & \vdots \\ \mathbf{0} & \mathbf{0} & \dots & \mathbf{R}_{\text{proc}} \end{bmatrix} \quad [31]$$

where \mathbf{R}_{proc} is the cumulative uncertainty caused by process noise for a single measurement. \mathbf{R}_{proc} has dependence on epoch t , system state $\mathbf{x}(t)$, and user-defined process noise $\mathbf{d}^{\mathcal{R}} = [\mathbf{d}_{\text{abs}}, \mathbf{d}_{\text{rel}}]^{\top} \in \mathbb{R}^6$. Process noise $\mathbf{d}^{\mathcal{R}}$ consists of perturbing accelerations in

4.2 Partial Measurement Availability

\mathcal{R} for the observer absolute orbit and target relative orbits. Typical approximate values in LEO are $\mathbf{d}_{\text{abs}} = 10^{-7}[1, 1, 1]$ m/s² and $\mathbf{d}_{\text{rel}} = 10^{-9}[1, 4, 1]$ m/s².

To compute \mathbf{R}_{proc} for bearing angle measurements, consider the combined time-varying orbit state and orbit covariance for an observer and target at t .

$$\begin{aligned} \mathbf{x}(t) &= [\boldsymbol{\alpha}(t), \delta\boldsymbol{\alpha}(t)] \in \mathbb{R}^{12} \\ \boldsymbol{\Sigma}(t) &= \begin{bmatrix} \boldsymbol{\Sigma}_{\boldsymbol{\alpha}} & \mathbf{0}^{6 \times 6} \\ \mathbf{0}^{6 \times 6} & \boldsymbol{\Sigma}_{\delta\boldsymbol{\alpha}} \end{bmatrix} \in \mathbb{R}^{12 \times 12} \end{aligned} \quad [32]$$

Given $\boldsymbol{\Sigma}(t)$, the propagated covariance $\boldsymbol{\Sigma}(t + \Delta t)$ is computed via

$$\begin{aligned} \boldsymbol{\Sigma}(t + \Delta t) &= \mathbf{A}(\mathbf{x}(t))\boldsymbol{\Sigma}(t)\mathbf{A}^\top(\mathbf{x}(t)) + \\ &\quad \mathbf{B}(\mathbf{x}(t)) \text{diag}(\mathbf{d}^{\mathcal{R}} \Delta t) \mathbf{B}^\top(\mathbf{x}(t)) \end{aligned} \quad [33]$$

where $\mathbf{A}(\mathbf{x}(t)) \in \mathbb{R}^{12 \times 12}$ is the time-varying state transition matrix [19] and $\mathbf{B}(\mathbf{x}(t))$ is the RTN control input matrix [28]. The state covariance due to dynamics uncertainty is initialized as $\boldsymbol{\Sigma}(t_0) = \mathbf{0}^{12 \times 12}$ at estimation epoch t_0 . At each subsequent epoch, $\boldsymbol{\Sigma}(t)$ is converted to $\mathbf{R}_{\text{proc}}(t)$ via an unscented transform from orbit states to bearing angles. In this fashion, \mathbf{R}_{dyn} captures increasing measurement uncertainty with time due to mismodeled dynamics and correlation of uncertainty with orbit state.

4.2 Partial Measurement Availability

To apply the numeric observability computation to a system, its topology is first generated via Algorithm 1. $\mathbf{M}(t)$ and \mathbf{P}_{est} can then be computed for each subsystem. However, recall from Section 3 that beacon status can propagate between observers: an observer j may rely on the absolute state estimate \mathbf{z}_i broadcast by remote beacon i to attain subsystem observability by itself. If so, \mathbf{R}_{meas} for \mathbf{z}_i is the absolute state uncertainty computed in \mathbf{P}_{est} for subsystem i . It is therefore necessary to compute subsystem \mathbf{P}_{est} estimates in order, such that subsystems reliant on remote state estimates from i compute their \mathbf{P}_{est} after i . Upon completion, all subsystem \mathbf{P}_{est} may be combined to produce a system-wide metric, such as worst-case uncertainty across all objects.

Furthermore, measurement availability throughout \mathbf{t}_m is often inconsistent due to varying inter-spacecraft geometry, sensor attitudes, and target visibility conditions. Numerical checks are performed at each epoch to confirm measurement availability. If unavailable, the corresponding row in \mathbf{Y}_{est} is removed. Physical measurement constraints are thus accounted for. Additionally, if no measurements are sensitive to a specific state component, the corresponding column in

| OE | a | e | i | Ω | ω | M_0 |
|-----|-------------|------------------|---------------|---------------|---------------|---------------|
| LEO | 6778 km | 0.001 | 98° | 0° | 0° | 0° |
| EEO | 13556 km | 0.5 | 98° | 0° | 0° | 0° |
| MEO | 20200 km | 0 | 55° | 0° | 0° | 0° |
| ROE | $a\delta a$ | $a\delta\lambda$ | $a\delta e_x$ | $a\delta e_y$ | $a\delta i_x$ | $a\delta i_y$ |
| EI | 0 | 100 km | 0 | 4 km | 0 | 4 km |
| IT | 0 | 100 km | 0 | 0.2 km | 0 | 0.2 km |
| CO | 0 | $2\pi a/N_s$ | 0 | 0 | 0 | $2\pi a/N_s$ |

Table 2: Orbit geometries for numerical analysis.

| Model | Perturbations | Propagation |
|----------|----------------------------------|--------------------------------|
| Kepler | None | Analytic |
| J_2 | J_2 gravity | Analytic |
| 5x5 | 5x5 spherical harmonic gravity | RK4 integrator 60s timestep |
| Complete | 20x20 spherical harmonic gravity | RK4 integrator 60s timestep |
| | Harris-Priester atmosphere | |
| | with cannonball drag model | |
| | Solar radiation pressure | |
| | with cannonball drag model | |
| | Third-body lunisolar gravity | |

Table 3: Dynamics models for numerical analysis.

\mathbf{Y}_{est} is removed to maintain numerical stability. Such state components are unobservable.

4.3 Numeric State Observability Assessment

To illustrate the numeric method, it is first useful to assess angles-only observability when varying estimated states and orbit geometries. Tables 2-4 present orbit geometries, dynamics models, and default hardware parameters. Absolute orbits include near-circular low Earth orbit (LEO), eccentric Earth orbit (EEO) and medium Earth orbit (MEO). Formations include an E/I-vector separated swarm (EI) at close inter-object separations with significant relative motion; an in-train formation (IT) at close separations with little relative motion; and a constellation (CO) at far separations with equally-spaced orbit planes and mean anomalies. Each formation consists of four observers $\{i, j, k, l\}$ such that the ROE between pairs $\{i, j\}$, $\{j, k\}$, $\{k, l\}$ are identical as per Table 2. The VBS consistently points in the (anti)-velocity direction for IT and EI cases, or cyclically points at each target in subsequent epochs for CO cases. Measurements are generated across two orbits with fifty equally-spaced measurements per orbit.

Results are presented in Table 5 for the complete dynamics model. The overbar denotes a mean uncertainty across all system objects, normalized by semimajor axis where appropriate. Column 1, where only the relative orbit is estimated, is expected to be 2nd-order LWO. Column 2, where absolute and rela-

4.4 Numeric Validation of Analytic Observability

| Parameter | Value |
|-----------------------------|---|
| Spacecraft mass | 50 kg |
| Spacecraft surface area | 1m ² |
| Spacecraft ballistic coeff. | 0.025 |
| VBS FOV | 12° × 10° |
| VBS detectable magnitude | 7.5 |
| VBS sun exclusion angle | 45° |
| VBS noise (1σ) | (20'', 20'') |
| GNSS position noise (1σ) | (10, 10, 10) m |
| GNSS velocity noise (1σ) | (0.02, 0.02, 0.02) m/s |
| ISL radio range | 2000 km |
| Process noise (absolute) | (10 ⁻⁷ , 10 ⁻⁷ , 10 ⁻⁷) ^R m/s ² |
| Process noise (relative) | (10 ⁻⁹ , 4 × 10 ⁻⁹ , 10 ⁻⁹) ^R m/s ² |
| Clock offset (initial) | 1 second |
| Clock drift rate (initial) | 1 μs/s |

Table 4: Default parameters for numeric analysis.

tive orbits are estimated, is expected to be 3rd-order LWO. Both cases are observable but the 3rd-order case is numerically weaker, as expected.

Column 3 introduces clock offset and drift estimation. Clock parameters are observable with bearing angles and furthermore, their inclusion has only minor effects on orbit uncertainty. Column 4 introduces ballistic coefficient estimation and although the coefficients are observable, uncertainty in a , δa and u increases because drag forces (which are dependent on ballistic coefficient) cause secular changes in the semimajor axis. Column 5 adds estimation of bearing angle sensor biases, for which azimuth biases are more observable. The $\delta\lambda$ ROE is itself analogous to an elevation bias caused by orbit curvature, and in near-circular orbits where $\delta\lambda$ is approximately constant, it is challenging to differentiate an elevation bias caused by the sensor itself.

Column 6 presents an IT formation for which observability is much weaker due to the reduced magnitude of relative motion. Measurements in this formation are close to improper with $\delta i \approx \delta e \approx \delta a \approx 0$. Column 7 presents an eccentric orbit for which observability is much stronger, due to the additional components of absolute and relative motion introduced by eccentricity [29]. Column 8 presents a constellation at far separations. Absolute orbit observability particularly benefits because the orbits and measurement baselines of each spacecraft are very distinct; resulting bearing angle geometries reduce ambiguities in localization, analogous to reducing ‘dilution of precision’ [30] in GNSS navigation. Relative orbit observability is not as strong because at larger target ranges, the same amount of bearing angle noise corresponds to a larger state uncertainty.

Overall, the numeric analysis demonstrates that it

| Rel. Orbit | EI | EI | EI | EI | EI | IT | EI | CO |
|--|-----|------|------|--------|--------|-------|--------|------|
| Abs. Orbit | LEO | LEO | LEO | LEO | LEO | LEO | EEO | MEO |
| $\overline{\sigma}_a$ (m) | - | 24 | 40 | 130 | 130 | 520 | 51 | 78 |
| $a\overline{\sigma}_{e_x}$ (m) | - | 270 | 270 | 270 | 270 | 15000 | 76 | 73 |
| $a\overline{\sigma}_{e_y}$ (m) | - | 310 | 340 | 350 | 350 | 15000 | 130 | 71 |
| $a\overline{\sigma}_i$ (m) | - | 570 | 570 | 570 | 580 | 6000 | 120 | 160 |
| $a\overline{\sigma}_{\Omega}$ (m) | - | 1100 | 1100 | 1100 | 1100 | 5900 | 250 | 230 |
| $a\overline{\sigma}_u$ (m) | - | 310 | 320 | 420 | 1400 | 44000 | 310 | 260 |
| $a\overline{\sigma}_{\delta a}$ (m) | 2 | 4 | 4 | 7 | 7 | 160 | 2 | 35 |
| $a\overline{\sigma}_{\delta\lambda}$ (m) | 190 | 350 | 350 | 410 | 760 | 5900 | 280 | 430 |
| $a\overline{\sigma}_{\delta e_x}$ (m) | 1 | 9 | 9 | 9 | 9 | 370 | 2 | 120 |
| $a\overline{\sigma}_{\delta e_y}$ (m) | 8 | 15 | 16 | 16 | 16 | 350 | 13 | 110 |
| $a\overline{\sigma}_{\delta i_x}$ (m) | 1 | 27 | 27 | 28 | 28 | 140 | 3 | 230 |
| $a\overline{\sigma}_{\delta i_y}$ (m) | 8 | 19 | 20 | 20 | 20 | 150 | 11 | 310 |
| $\overline{\sigma}_{\delta c_{err}}$ (ms) | - | - | 35 | 36 | 510 | 12000 | 97 | 110 |
| $\overline{\sigma}_{\delta d_{err}}$ ($\frac{\mu s}{s}$) | - | - | 3.0 | 3.2 | 3.2 | 3.2 | 1.9 | 1.7 |
| $\overline{\sigma}_{\delta B_{ATM}}$ | - | - | - | 0.0062 | 0.0062 | 0.018 | - | - |
| $\overline{\sigma}_{\delta B_{err}}$ | - | - | - | - | - | - | 0.0012 | 0.16 |
| $\overline{\sigma}_{b_a}$ (") | - | - | - | - | 0.4 | 0.4 | 0.5 | 0.4 |
| $\overline{\sigma}_{b_e}$ (") | - | - | - | - | 14 | 450 | 1.1 | 0.5 |

Table 5: Estimated 1-σ state uncertainty for varying state components and orbit geometry.

is possible to estimate orbit and auxiliary state components using angles-only measurements. However, orbit geometry significantly affects observability and must be taken into account. The strongest observability results are encountered when motion of targets in the bearing angle state space is highly nonlinear, geometrically distinct, and large in magnitude.

4.4 Numeric Validation of Analytic Observability

The numeric method is next applied to validate the topological observability conditions of Algorithm 1. All possible two- and three-spacecraft systems are enumerated and the numeric observability of proper systems fulfilling at least one observability condition is compared to observability of improper systems which do not. The set of systems consisting of N_s objects is enumerated by considering all possible assignments of sets \mathcal{T}_i and \mathcal{C}_i for $i \in \{1, 2, \dots, N_s\}$, where $i \in \mathcal{T}_i$ implies i is an external beacon and $i \notin \mathcal{C}_i$. After combining topologically identical cases and discarding trivial cases, there exists 13 unique two-object systems and 322 unique three-object systems. Of these, 232 are expected to be observable via Algorithm 1.

Table 6 presents minimum and maximum numeric orbit uncertainties for proper versus improper systems. In the majority of cases, the maximum orbit uncertainty of a proper system is orders of magnitude smaller than the minimum orbit uncertainty of an improper system. Exceptions are observed for IT systems which possess large uncertainties despite being topologically proper; this is because the measurements themselves are very close to improper. A separate exception is the constellation. The minimum uncertainty for improper systems (occurring when

5. Observability Optimization

| Orbit Abs. | Rel. | Dynamics | Orbit Uncertainty (% of a) | |
|---------------|------|----------|-------------------------------|------------------|
| | | | Proper System | Improper System |
| LEO | EI | Kepler | [0.00003, 0.04291] | [13.94, 5696] |
| LEO | EI | J_2 | [0.00003, 0.04203] | [13.94, 1069] |
| LEO | EI | 5x5 | [0.00003, 0.04197] | [12.99, 838.9] |
| LEO | EI | Complete | [0.00003, 0.04197] | [12.87, 826.8] |
| LEO | IT | Kepler | [0.00003, 3.352] | [14750, 103000] |
| EEO | EI | Kepler | [0.00001, 0.00599] | [0.3544, 3.728] |
| MEO | CO | Kepler | [0.00001, 0.00490] | [0.00592, 60.06] |

Table 6: Numeric orbit uncertainty ranges for proper vs. improper systems.

$N_m = N_s - 1$, as per Row 5 in Table 1) is only slightly larger than the maximum uncertainty for proper systems (occurring when $N_m = N_s$, as per Row 6 in Table 1). Constellations in general possess stronger observability, and this result perhaps indicates the presence of a 4th-order or above analytic LWO condition for three object-systems when $N_m = N_s - 1$. Results also show the expected trend of additional dynamics perturbations improving observability.

Finally, it is useful to characterize the strengths of angles-only analytic observability conditions presented both here and in prior work. Consider four system ‘types’, conceptually illustrated in Figure 7 for four spacecraft. To estimate N_s states,

1. Type 1 uses $N_s - 1$ observers to produce a chain of $N_s - 1$ angles
2. Type 2 uses N_s observers to produce a loop of N_s angles
3. Type 3 uses two observers with one shared target to produce N_s angles
4. Type 4 uses two observers with $N_s - 2$ shared targets to produce $2N_s - 2$ angles

This paper considers Type 3 and Type 4 systems with $N_s \geq 3$ observable; Type 2 systems with $N_s = 3$ observable; and Type 1 systems unobservable via Algorithm 1. Type 2 systems with $N_s > 3$ are invalidated by the communication limitations imposed by the topology definition. Work by Hu et al. [13] which assumes global communication considers such systems valid and observable and proposes Type 1 systems with $N_s \geq 4$ are analytically observable also.

Table 7 presents a comparison of system types. In practice, Type 1 systems are only numerically observable for the constellation; observability remains poor for Type 1 EI and IT swarms, even for $N_s \geq 4$. Results for Type 3 and Type 4 systems are consistent and follow expected trends in that additional measurements reduce orbit uncertainty. Type 2 systems

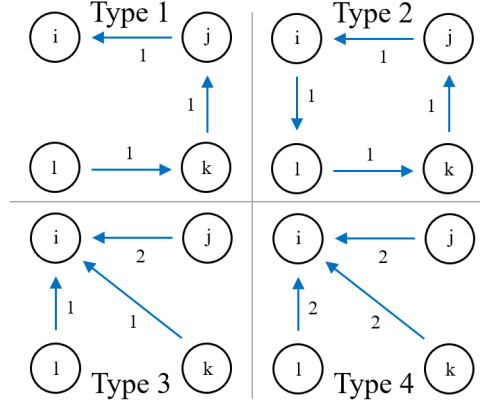


Fig. 7: Four topology types for a four-object system.

| Type | Members | Measurements | EI | EI | CO |
|------|--------------------|-------------------------------|-------------------------------|--------|--------|
| | | | LEO | LEO | MEO |
| | | | 5x5 | Kepler | Kepler |
| | | | Orbit Uncertainty (% of a) | | |
| 1 | i, j | z_{ji} | 396 | 2860 | 6.1 |
| 1 | i, j, k | $z_{ji,kj}$ | 15.0 | 16.1 | 0.0072 |
| 1 | i, j, k, l | $z_{ji,kj,lk}$ | 13.0 | 14.0 | 0.0058 |
| 1 | i, j, k, l, m | $z_{ji,kj,lk,ml}$ | 10.6 | 11.4 | 0.0058 |
| 1 | i, j, k, l, m, n | $z_{ji,kj,lk,ml,nm}$ | 9.7 | 10.4 | 0.0057 |
| 2 | i, j | $z_{ji,ij}$ | 379 | 1890 | 4.32 |
| 2 | i, j, k | $z_{ji,kj,ik}$ | 0.042 | 0.043 | 0.0050 |
| 2 | i, j, k, l | $z_{ji,kj,lk,il}$ | 0.999 | 1.005 | 0.0043 |
| 2 | i, j, k, l, m | $z_{ji,kj,lk,ml,im}$ | 0.034 | 0.035 | 0.0045 |
| 2 | i, j, k, l, m, n | $z_{ji,kj,lk,ml,nm,in}$ | 0.498 | 0.500 | 0.0043 |
| 3 | i, j, k | $z_{ji,ki,jk}$ | 0.042 | 0.043 | 0.0050 |
| 3 | i, j, k, l | $z_{ji,ki,li,jl}$ | 0.034 | 0.035 | 0.0039 |
| 3 | i, j, k, l, m | $z_{ji,ki,li,mi,jm}$ | 0.030 | 0.031 | 0.0037 |
| 4 | i, j, k | $z_{ji,ki,jk,ik}$ | 0.036 | 0.037 | 0.0043 |
| 4 | i, j, k, l | $z_{ji,ki,li,kl,jl,il}$ | 0.028 | 0.029 | 0.0033 |
| 4 | i, j, k, l, m | $z_{ji,ki,li,mi,lm,km,jm,im}$ | 0.024 | 0.024 | 0.0029 |

Table 7: Maximum estimated orbit uncertainty for the given system and measurement set.

possess less consistency. For the EI/LEO case, systems with even N_s encounter comparatively larger uncertainty due to a weakly observable mode that manifests when the ROE ratios $\delta e_{x,y}/\delta \lambda$ and $\delta i_{x,y}/\delta \lambda$ are identical between all objects. Introducing a unique ROE ratio between one object pair removes the mode.

Overall, numeric analysis suggests that the topological conditions of Algorithm 1 are sufficient for complete system orbit observability. Proper systems fulfilling the conditions display physically consistent observability trends regardless of orbital configuration or dynamics model fidelity.

5. Observability Optimization

DSS must achieve a certain level of state estimation accuracy to allow fulfilment of mission objectives. For angles-only systems with complex rela-

5.1 Design State Space

tionships between system parameters and navigation performance, these requirements must be specifically addressed during the system design phase. This section places the analytic and numeric methods from Sections 3 and 4 within an optimization framework to propose a proof-of-concept method for flexible, automatic optimization of system observability in accordance with designer preferences.

5.1 Design State Space

In results thus far, five core system properties have been found to affect observability:

1. The number of unique bearing angle edges accessible by the observer, as per the the sum of relevant edge weights in its subsystem topology.
2. The number of bearing angle measurements received for each edge throughout the measurement period, as per the rows in \mathbf{Y}_{est} .
3. The sensitivity of each received bearing angle measurement to the subsystem state and its variability and nonlinearity throughout the measurement period, as expressed in \mathbf{Y}_{est} .
4. The amount of measurement noise and uncertainty, as expressed in \mathbf{R} .
5. The estimated state components, as per the columns in \mathbf{Y}_{est} .

Each is dependent on physical aspects of the system. The measurement topology is affected by the number of active observers and passive targets within the system and which targets prove navigable by which observers, as influenced by orbit geometry, sensor hardware and attitude, target visibility, and ISL communication range. The number of bearing angle measurements received in total likewise depends on these parameters as well as the measurement frequency and total measurement period. The variability and nonlinearities present in bearing angle measurements are dependent on orbit geometry and absolute and differential dynamics. Measurement noise is influenced by both sensor and process noise. The state space for optimization is therefore complex and to limit problem scope, two specific case studies for DSS design in lunar orbit are defined as follows. The lunar scenario is of interest due to its variety of potential near-future applications [10] and challenges of employing external localization methods such as GNSS or DSN measurements.

5.2 Case Study 1

Consider a swarm of spacecraft performing distributed science operations in a quasi-frozen low lunar orbit [31]. It is desired to estimate the absolute orbit, relative orbit and clock parameters of each swarm member using angles-only methods. Science and collision avoidance requirements specify initial nominal OE and allowable ROE ranges of

$$\begin{aligned}\boldsymbol{\alpha} &= [1850 \text{ km}, -0.0482, 0.0120, 89^\circ, 166^\circ, 270^\circ]^\top \\ \delta\boldsymbol{\alpha}_{\text{min}} &= [0, 40 \text{ km}, 0, 1000 \text{ m}, 0, 1000 \text{ m}]^\top \\ \delta\boldsymbol{\alpha}_{\text{max}} &= [0, 60 \text{ km}, 0, 4000 \text{ m}, 0, 4000 \text{ m}]^\top\end{aligned}$$

Across the system, define the worst-case observer absolute position uncertainty $\boldsymbol{\Sigma}_{\mathbf{r}} \in \mathbb{R}^3$; worst-case target relative position uncertainty $\boldsymbol{\Sigma}_{\delta\mathbf{r}} \in \mathbb{R}^3$; and worst-case differential clock uncertainty $\Sigma_{\delta c_{\text{err}}}$. To meet mission requirements, the system must fulfil

$$\begin{aligned}\|\boldsymbol{\Sigma}_{\mathbf{r}}\|_2 &< \Sigma_{\mathbf{r}}^{\text{goal}} = 100 \text{ m} \\ \|\boldsymbol{\Sigma}_{\delta\mathbf{r}}\|_2 &< \Sigma_{\delta\mathbf{r}}^{\text{goal}} = 50 \text{ m} \\ \Sigma_{\delta c_{\text{err}}} &< \Sigma_{\delta c_{\text{err}}}^{\text{goal}} = 100 \text{ ms}\end{aligned}$$

using two orbits of measurements.

For simplicity, it is assumed ROE between each pair of neighboring objects (with respect to u) are identical. Physical parameters of each object are also assumed identical with default values as per Table 4. Observers and targets are arranged such that passive targets are in the center of the swarm with respect to u ; half of the observers fly ahead of passive targets with VBS pointed in the anti-velocity direction and half of the observers fly behind passive targets with VBS pointed in the velocity direction. For swarm members in sufficiently similar orbits this arrangement produces the most possible bearing angle edges without requiring active target pointing. Figure 8 presents a schematic.

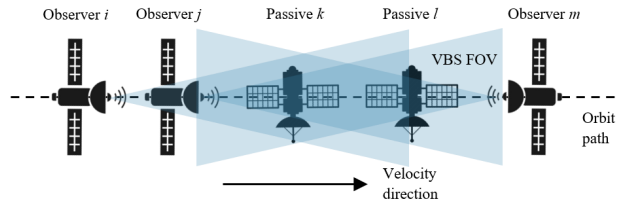


Fig. 8: A notional schematic of a five-member swarm. ‘Neighbors’ are pairs $\{i, j\}$, $\{j, k\}$, and so on.

Parameters p_i to be optimized are displayed in Table 8. Each is constrained to a valid interval $g_i =$

5.3 Case Study 2

| Parameter | Description | Valid Interval | Step Size |
|-----------|------------------------------|-------------------|------------|
| p_1 | Number of observers | [1, 10] | 1 |
| p_2 | Number of passive targets | [0, 10] | 1 |
| p_3 | $\delta\lambda$ | [10, 100] km | 1 km |
| p_4 | $\delta e_y / \delta\lambda$ | [0, 0.1] | 0.001 |
| p_5 | $\delta i_y / \delta\lambda$ | [0, 0.1] | 0.001 |
| p_6 | VBS FOV | [10, 90] $^\circ$ | 1 $^\circ$ |
| p_7 | VBS detectable magnitude | [5, 10] | 0.1 |
| p_8 | VBS measurement noise | [5, 30] $''$ | 1 $''$ |
| p_9 | Process noise factor | [10 $^{-3}$, 10] | 10 $^{-3}$ |
| p_{10} | Measurement frequency | [60, 300] sec | 5 sec |
| p_{11} | Communication range | [200, 10000] km | 100 km |
| p_{12} | VBS per observer | [1, 2] | 1 |

Table 8: Optimization variables for Case Study 1.

$[l_i, u_i]$ discretized by step size Δp_i . It is assumed $\delta a = \delta e_x = \delta i_x = 0$ to further simplify formation optimization. ‘Process noise factor’ refers to a multiplicative factor for the default process noise in Table 4, to emulate the inclusion of more accurate but more computationally intensive dynamics models on board. ‘VBS per observer’ allows for placing two sensors on each observer to simultaneously view the velocity and anti-velocity directions. It is elected to discretize the entire state space for consistency because some parameters (such as p_1 and p_2) are discrete by definition.

5.3 Case Study 2

Consider a DSS performing wide-coverage SSA operations in a lunar flower constellation [32]. It is desired to estimate the absolute orbit, relative orbit and clock parameters of each constellation member using angles-only methods. The constellation consists of N_p orbit planes separated equidistantly in Ω . Within each plane, spacecraft are separated equidistantly in u . Inclination i is variable. Other absolute OE are constant with $a = 5054$ km; $e = 0.6067$; $\omega = 0^\circ$. Figure 9 presents a schematic for $i = 60^\circ$. To meet mission requirements, estimated navigation performance must fulfill

$$\begin{aligned} \|\Sigma_r\|_2 &< 50 \text{ m} \\ \|\Sigma_{\delta r}\|_2 &< 100 \text{ m} \\ \Sigma_{\delta c_{\text{err}}} &< 100 \text{ ms} \end{aligned}$$

using two orbits of measurements and for redundancy, the system must maintain this performance upon the loss of any single member. The physical parameters of each observer are assumed identical with default values as per Table 4. To track visible targets in different orbit planes with limited sensor FOV, observers are required to actively point their VBS at their targets in a cyclic fashion throughout the mea-

| Parameter | Description | Valid Interval | Step Size |
|-----------|--------------------------|--------------------|------------|
| p_1 | Observers per plane | [1, 6] | 1 |
| p_6 | VBS FOV | [30, 120] $^\circ$ | 1 $^\circ$ |
| p_7 | VBS detectable magnitude | [7, 12] | 0.1 |
| p_8 | VBS measurement noise | [5, 30] $''$ | 1 $''$ |
| p_9 | Process noise factor | [10 $^{-3}$, 10] | 10 $^{-3}$ |
| p_{10} | Measurement frequency | [300, 900] sec | 10 sec |
| p_{11} | Communication range | [2000, 20000] km | 100 km |
| p_{13} | Number of orbit planes | [1, 6] | 1 |
| p_{14} | Orbit plane inclination | [30, 90] $^\circ$ | 1 $^\circ$ |

Table 9: Optimization variables for Case Study 2.

surement period. Parameters to be optimized are displayed in Table 9.

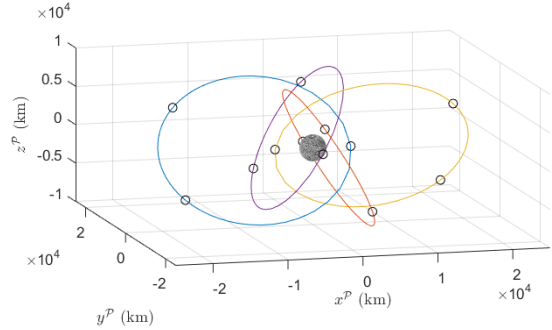


Fig. 9: A notional schematic of a four-plane constellation with three observers (circles) per plane.

5.4 Cost Function Formulation

Denote the system design state space as \mathbb{P} for an output design $\mathbf{p} \in \mathbb{P}$. The goal of the optimization is to optimize \mathbf{p} with respect to a defined cost. This cost is related to a navigation performance metric where here, the basic navigation cost J_Σ is defined quadratically as

$$J_\Sigma(\mathbf{p}) = \Sigma_r^\top \mathbf{Q}_r \Sigma_r + \Sigma_{\delta r}^\top \mathbf{Q}_{\delta r} \Sigma_{\delta r} + Q_{\delta c_{\text{err}}} \Sigma_{\delta c_{\text{err}}}^2 \quad [34]$$

with weighting terms $\mathbf{Q}_r, \mathbf{Q}_{\delta r} \in \mathbb{R}^{3 \times 3}$ and $Q_{\delta c_{\text{err}}}$. In this paper, $\mathbf{Q}_r = \mathbf{Q}_{\delta r} = \mathbf{I}_3$ and $Q_{\delta c_{\text{err}}} = v_{\text{max}}^2$, where v_{max} is the maximum orbit velocity observed during the measurement period. Worst-case rather than mean navigation performance is optimized to ensure all system members meet the required performance goal. More generally, it is necessary to balance multiple costs: for example, adding another observer may improve observability but presents a non-trivial implementation cost. Practical constraints may make it be preferable to minimize the number of spacecraft or maintain a desired set of ROE as closely as possible. Additional cost terms must then be added to total

5.5 Optimization Method

cost $J(\mathbf{p})$. Examples are provided below which may be modified to suit user preferences.

Define a system cost function $J(\mathbf{p})$ as

$$J(\mathbf{p}) = J_{\text{plane}}(J_{\text{obs}} + J_{\text{tar}}) + J_{\text{nom}} + J_{\text{goal}} \quad [35]$$

which accounts for costs of additional orbit planes J_{plane} ; observers per plane J_{obs} ; passive targets per plane J_{tar} ; deviation from nominal ROE J_{nom} ; and failure to meet goal performance J_{goal} . Observer cost consists of various hardware costs and is defined as

$$J_{\text{obs}}(\mathbf{p}) = Q_{N_o} N_o (1 + J_{\text{vbs}} + J_{\text{isl}} + J_{\text{cpu}}) J_{\Sigma} \quad [36]$$

where N_o is the number of observers, Q_{N_o} is a weighting factor and J_{vbs} , J_{isl} , J_{cpu} are costs related to the optical sensor, ISL radio, and onboard processor respectively. The weighting factor is

$$Q_{N_o+1} = \frac{Q_{N_o}}{(1-f_o)} \frac{N_o}{N_o+1} \quad \text{with} \quad Q_1 = 1 \quad [37]$$

This definition encodes the desired navigation performance benefit of adding an additional observer in $0 < f_o < 1$. For example, choosing $f_o = 0.2$ ensures adding one observer must reduce J_{Σ} by at least 20% to improve cost J_{obs} . Similarly,

$$J_{\text{plane}}(\mathbf{p}) = Q_{N_p} N_p \quad J_{\text{tar}}(\mathbf{p}) = Q_{N_t} N_t J_{\Sigma} \quad [38]$$

$$Q_{N_p+1} = \frac{Q_{N_p}}{(1-f_p)} \frac{N_p}{N_p+1} \quad Q_{N_t+1} = \frac{Q_{N_t}}{(1-f_t)} \frac{N_t}{N_t+1} \quad [39]$$

This paper applies $f_o = 0.35$; $f_t = 0.25$; $f_p = 0.75$. Constituent terms of J_{obs} are defined as

$$J_{\text{vbs}} = p_{12} \left(Q_{\text{fov}} \frac{p_4}{30^\circ} + Q_{\text{mag}} \frac{p_5}{7} + Q_{\text{meas}} \frac{20''}{p_6} \right) \quad [40]$$

$$J_{\text{cpu}} = Q_{\text{proc}} \frac{1}{p_7} + Q_{\text{freq}} \frac{120 \text{ s}}{p_8} \quad [41]$$

$$J_{\text{isl}} = Q_{\text{comm}} \frac{p_9}{2000 \text{ km}} \quad [42]$$

In order, each term accounts for the cost of sensors per observer; sensor FOV; sensor detectable magnitude; sensor measurement noise; dynamics process noise; measurement frequency; and radio communication range, via simple proportional functions. More realistic dependencies can be implemented given knowledge of available hardware options. This paper applies weightings $Q_{\text{fov}} = 0.1$; $Q_{\text{meas}} = Q_{\text{mag}} = 0.2$; $Q_{\text{comm}} = Q_{\text{freq}} = 0.05$; $Q_{\text{proc}} = 0.001$.

To define ROE cost penalties, consider a range of nominal ROE defined by minimum ROE $\delta\alpha_{\text{min}}$ and maximum ROE $\delta\alpha_{\text{max}}$. Penalized ROE lying outside this range are found via the elementwise maximum

$\delta\alpha_{\text{pen}} = \max(\mathbf{0}, \delta\alpha_{\text{min}} - \delta\alpha, \delta\alpha - \delta\alpha_{\text{max}})$. The ROE cost penalty is defined quadratically as

$$J_{\text{nom}}(\mathbf{p}) = N_p (N_o + N_t) \delta\alpha_{\text{pen}}^\top \mathbf{Q}_{\text{nom}} \delta\alpha_{\text{pen}} \quad [43]$$

where $\mathbf{Q}_{\text{nom}} \in \mathbb{R}^{6 \times 6}$ is a weighting matrix determining penalization of specific ROE. This paper applies $\mathbf{Q}_{\text{nom}} = \text{diag}(100, 0.01, 1, 1, 1, 1)$ m. Finally, the navigation performance penalty is defined by

$$J_{\text{goal}}(\mathbf{p}) = Q_{\mathbf{r}}^{\text{goal}} \max(0, \|\Sigma_{\mathbf{r}}\|_2 - \Sigma_{\mathbf{r}}^{\text{goal}})^2 \\ + Q_{\delta\mathbf{r}}^{\text{goal}} \max(0, \|\Sigma_{\delta\mathbf{r}}\|_2 - \Sigma_{\delta\mathbf{r}}^{\text{goal}})^2 \\ + Q_{\delta c_{\text{err}}}^{\text{goal}} \max(0, \|\Sigma_{\delta c_{\text{err}}}\|_2 - \Sigma_{\delta c_{\text{err}}}^{\text{goal}})^2 \quad [44]$$

This paper applies weights of $Q_{\mathbf{r}}^{\text{goal}} = Q_{\delta\alpha}^{\text{goal}} = Q_{\delta c_{\text{err}}}^{\text{goal}} = 10^3$ to penalize the design towards achieving the navigation performance constraint.

Recall that the valid design domain \mathbb{P} is limited to intervals $g_i = [l_i, u_i]$ as in Tables 8-9. Solutions are therefore subject to a vector of box constraints $\mathbf{l} \leq \mathbf{p} \leq \mathbf{u}$. The optimization problem is expressed as

$$\begin{aligned} & \min_{\mathbf{p} \in \mathbb{P}} J(\mathbf{p}) \\ & \text{s.t. } \mathbf{l} \leq \mathbf{p} \leq \mathbf{u} \end{aligned} \quad [45]$$

where the problem constraints and domain are convex. However, the cost function is non-convex because state uncertainties Σ in J_{Σ} are not convex functions of \mathbf{p} . This can be verified by numeric computation of the Hessian which is not always positive definite for the given problem. Convergence to the global minimum is therefore not guaranteed but can be encouraged with a suitable optimization method.

5.5 Optimization Method

Given some design initialization $\mathbf{p}^0 \in \mathbb{P}$, the resulting graph topology \mathcal{G}^0 is computed as per Section 3 and is tested for analytic observability via Algorithm 1. If unobservable, parameters are increased via $p_i \leftarrow p_i + 0.1(u_i - l_i)$ for $i = 1, 6, 7, 10, 11$, until constraints become active, and the graph and its analytic observability are recomputed. This parameter set aims to improve connectivity by increasing the total number of measurements and graph edges potentially available to observers. Numeric optimization commences once an observable initialization is found. At iteration k , $J_{\Sigma}(\mathbf{p}^k)$ is computed using the numeric method of Section 4 and the result is used to compute system cost $J(\mathbf{p}^k)$. It is then necessary to compute a descent direction γ^k and step size α^k which sufficiently reduce the cost function and converge towards a local cost minimum.

5.6 Optimization Results

The Broyden-Fletcher-Goldfarb-Shanno (BFGS) algorithm [33] is used to compute γ^k . BFGS is chosen because it is a quasi-Newton method which incorporates curvature information to accelerate convergence. Quasi-Newton methods also require fewer function evaluations than true Newton methods by approximating the Hessian with first-order information. To incorporate box constraints, the projected quasi-Newton BFGS (PQN-BFGS) algorithm proposed by Kim et al. [34] is applied. PQN-BFGS determines which variables are free (to be optimized over) or fixed (to remain unchanged) at each iteration and projects the quasi-Newton descent step onto the convex set prescribed by $\mathbf{l} \leq \mathbf{p} \leq \mathbf{u}$. Gradients are computed using central differences and the step sizes in Tables 8-9. Inexact line search is used to choose α^k , applying the standard Wolfe conditions [33] to assess step validity. The initial guess for α^k at each iteration is that which changes the integer parameter with the steepest gradient (i.e. $p_{1,2,13}$) by ± 1 ; if the Wolfe conditions are violated, the next guess for α^k is doubled or halved as appropriate. Optimization terminates when the minimum allowed discrete step size cannot decrease cost.

Note that the problem structure violates the conditions required for BFGS to converge to a global minimum. Firstly, the state space is discretized rather than continuous, implying a reduction in quality of the Hessian approximation. However, for the case studies above, the discretization retains convergent properties. Secondly, BFGS cannot guarantee reaching a global minimum for non-convex problems in which other critical points such as saddle points or local minima exist. Some optimization algorithms have been explicitly developed for enhanced performance in non-convex scenarios [35], but even so, convergence to a global minimum cannot be guaranteed in general. It is instead suggested here to augment BFGS with a post-convergence ‘exploration’ step motivated by insights into where local minima are likely to occur. Consider a system for which a local minimum exists at \mathbf{p}_a and a global minimum exists at \mathbf{p}_b , such that $p_{a,1} = 6; p_{b,1} = 7; p_{a,7} = 2; p_{b,7} = 2.4$; and $p_{a,i} = p_{b,i}$ for all other parameters (Figure 10). Conceptually, \mathbf{p}_b adds another observer to improve connectivity and observability, but for the new measurements to become accessible and improve system cost, each VBS must be able to detect fainter targets. When at local minimum \mathbf{p}_a , however, BFGS may naively test some $p_7^k = p_{a,7} + 0.1$ and determine that increasing p_7 cannot decrease cost. Physical aspects such as target visibility lead to discontin-

uous mappings between hardware parameters, measurement availability, and system cost which prove challenging for first- and second-order methods to traverse. In response, at each iteration, the algorithm is instructed to explore in two directions using $p_1^{k+1} \leftarrow p_1^k \pm 1$ and $p_i^{k+1} \leftarrow p_i^k \pm 0.1(u_i - l_i)$ for $i = 6, 7, 10, 11$. This ensures any potential benefits of an additional observer and its measurements are taken advantage of by improved hardware. Constellations encounter additional discontinuities created by the unpredictable visibility of targets in separate orbit planes; thus, another exploration step of $p_1^{k+1} \leftarrow p_1^k \mp 2$ and $p_{13}^{k+1} \leftarrow p_{13}^k \pm 2$ is added to examine potential benefits of dividing fewer observers among more planes. This level of exploration was empirically chosen by examining the problem state space. Algorithm 2 presents pseudocode for the optimization.

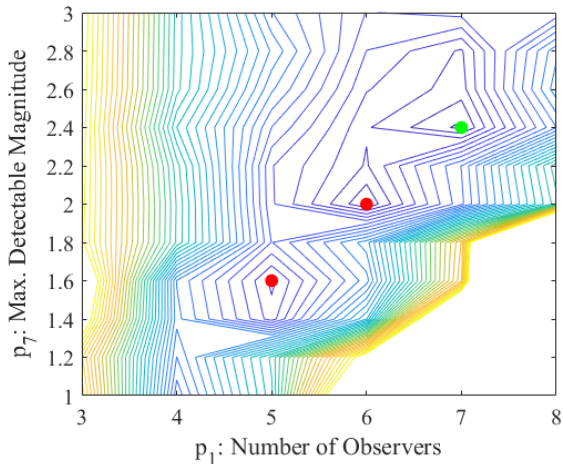


Fig. 10: A contour plot of system cost with local minima (red) and global minima (green).

5.6 Optimization Results

Table 10 presents optimal design parameters for Case Studies 1 and 2, confirmed to be global optima via state space sampling. For the applied cost function weightings, the swarm in Case 1 converges to four active observers with four passive targets. Passive targets remain useful because they provide additional measurement edges while being less costly than adding an active observer. This configuration also suggests the concept of using large spacecraft carrying science instruments to deploy small observer spacecraft carrying VBS which provide cooperative real-time orbit determination. ROE converge to the

5.6 Optimization Results

Algorithm 2: Observability optimization.

Data: Initial design parameters \mathbf{p}^0

Result: Optimal design parameters \mathbf{p}^*

1. Compute \mathcal{G}^0 and assess analytic observability.
 2. While \mathcal{G}^0 infeasible:
 - (a) $p_i^0 \leftarrow p_i^0 + 0.1(u_i - l_i) \forall i \in \{1, 6, 7, 10, 11\}$
 - (b) Recompute \mathcal{G}^0 and assess observability
 - (c) If all constraints are active, report failure
 3. Initialize second-order gradient scaling matrix $\mathbf{S}^0 \leftarrow \mathbf{I}$, system cost $J^0 \leftarrow J(\mathbf{p}^0)$, counter $k \leftarrow 0$
 4. While $J^{k+1} < J^k$:
 - (a) Compute projection $\Omega(\mathbf{p})$ of \mathbf{p}^k onto $[\mathbf{l}, \mathbf{u}]$
 - (b) Compute gradient $\nabla J(\mathbf{p}^k)$
 - (c) Compute fixed and free parameter sets [34]
 - (d) Compute α_k using line search with Wolfe conditions
 - (e) Compute $\mathbf{p}^{k+1} \leftarrow \Omega[\mathbf{p}^k - \alpha^k \mathbf{H}^k \nabla J(\mathbf{p}^k)]$
 - (f) Compute \mathbf{S}^{k+1} via PQN-BFGS update [34]
 - (g) Compute $J^{k+1} \leftarrow J(\mathbf{p}^{k+1})$
 - (h) Perform exploration:
 - i. Compute J for $p_1^{k+1} \pm 1$ with $p_i^{k+1} \pm 0.1(u_i - l_i) \forall i \in \{6, 7, 10, 11\}$
 - ii. If constellation: compute J for $p_1^{k+1} \mp 2$ and $p_{13}^{k+1} \pm 2$
 - (i) If exploration cost less than updated cost: update \mathbf{p}^{k+1} and J^{k+1}
 - (j) $k \leftarrow k + 1$
 5. Return \mathbf{p}^*
-

formation which produces the most relative motion while remaining within the nominal ROE range. Hardware parameters such as VBS FOV, detectable magnitude, and ISL range converge to the minimum values which enable complete graph connectivity. There is a strong preference towards reducing measurement noise and process noise to increase the observability of changes in state with respect to changes in measurements. The final estimated state uncertainties significantly improve over the performance goal and all constraints are successfully fulfilled.

The constellation in Case 2 converges to three active observers and three orbit planes. Any fewer observers per plane creates risks of temporary unobservability due to visibility constraints, whereas more observers per plane produces relatively limited improvements to observability. Similarly, three orbit planes with a 70° inclination balances the number of visible targets at each epoch, the amount of relative motion between planes, and the high cost of additional planes. The optimal VBS FOV and maximum de-

| Parameter | Description | Case 1 | Case 2 |
|----------------------------------|------------------------------|------------|-------------|
| p_1 | Number of observers | 4 | 3 |
| p_2 | Number of passive targets | 4 | - |
| p_3 | $\delta\lambda$ | 40 km | - |
| p_4 | $\delta e_y / \delta\lambda$ | 0.1 | - |
| p_5 | $\delta i / \delta\lambda$ | 0.1 | - |
| p_6 | VBS FOV | 19° | 112° |
| p_7 | VBS detectable magnitude | 4.7 | 11.6 |
| p_8 | VBS measurement noise | $5''$ | $5''$ |
| p_9 | Process noise factor | 0.05 | 0.12 |
| p_{10} | Measurement frequency | 90 sec | 360 sec |
| p_{11} | Communication range | 400 km | 7400 km |
| p_{12} | VBS per observer | 1 | 1 |
| p_{13} | Number of orbit planes | - | 3 |
| p_{14} | Orbit plane inclination | - | 78° |
| Σ_α | Abs. position uncertainty | 37 m | 19 m |
| $\Sigma_{\delta\alpha}$ | Rel. position uncertainty | 19 m | 38 m |
| $\Sigma_{\delta c_{\text{err}}}$ | Rel. clock uncertainty | 6 ms | 21 ms |

Table 10: Optimal design parameters and navigation performance after automatic optimization.

tectable magnitude are much larger than the swarm case to account for farther inter-object separations and extreme radial and cross-track motion. These values are not necessarily realistic for typical spaceborne cameras which may have FOV of $<30^\circ$ and a maximum detectable magnitude of ~ 7.5 . Nevertheless, all performance goals and constraints are successfully fulfilled, including navigational redundancy of any one system member.

Figure 11 presents cost progression for 20 random design initializations. For 50 tested random initializations, the applied framework produces adequate performance in that the global optimum is consistently found. Exploration is necessary to find the global optimum, however, with approximately 20% of swarm cases requiring exploration and 80% of constellation cases requiring exploration. Both scenarios are therefore non-convex, although local minima and discontinuities prove somewhat less prominent for the swarm. The swarm also presents more consistent trends in that higher initial costs imply more iterations before convergence with similarities in cost gradients across different initializations. In general, swarm geometry produces more limited relative motion with significantly more predictability in regards to which measurements are available to which observers. Constellation geometry and eccentric orbits produce more extreme relative motion with irregular functional relationships between design parameters and measurement availability. Furthermore, note that the minimum system cost does not correspond to the minimum navigation cost for the swarm and slightly higher state uncertainty with cheaper hard-

6. Conclusion

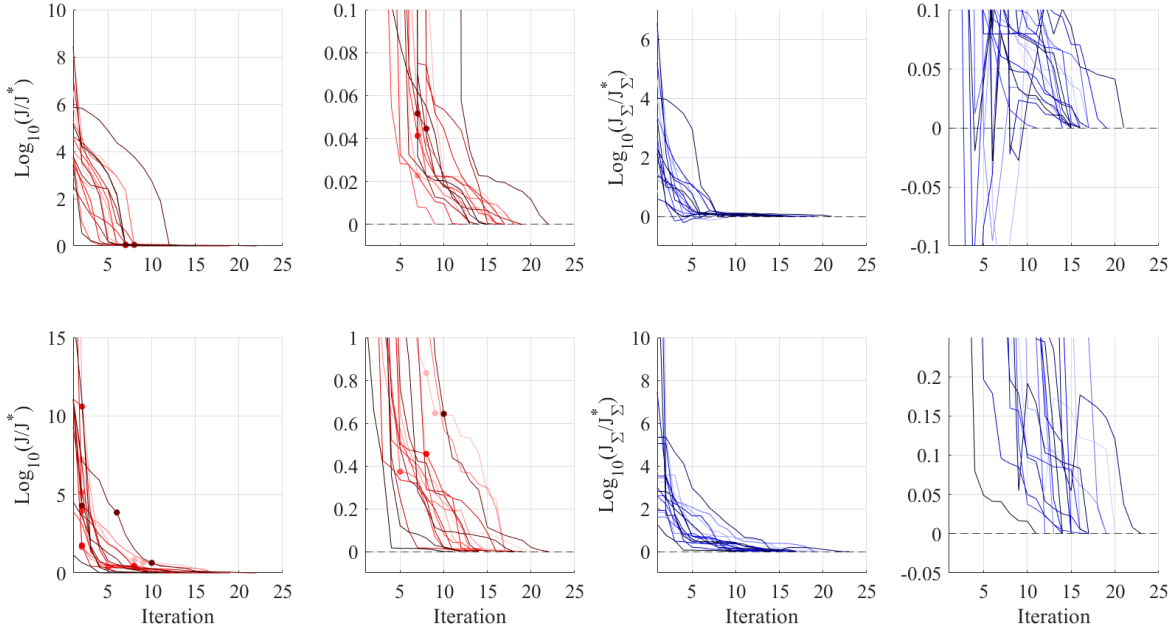


Fig. 11: Cost progressions for 20 random initializations of Case 1 (top) and Case 2 (bottom) towards globally optimal cost J^* and its corresponding J_{Σ}^* . Explore steps are marked by circles.

ware results in the lowest total system cost.

The successful application of automatic optimization to two different scenarios demonstrates that it is possible to leverage topological, analytic and numeric methods for effective observability-aware space system design under realistic dynamics and constraints. However, given the wide range of possible design parameters, cost tunings and mission scenarios, it is desirable to be able to guarantee convergence to a global minimum. Future work will focus on formulating a convex reduced-order model which captures the underlying nonlinear observability trends of angles-only space systems, to which convex optimization techniques can be applied. The accuracy of output uncertainty estimates will also be characterized via comparison to high-fidelity simulations using the ARTMS navigation architecture [9].

6. Conclusion

This paper constructs a set of unified observability analysis and design optimization tools for angles-only navigation of distributed space systems. To analytically determine whether a system is observable, a system graph topology representation is developed. The topology accounts for limited communication, visi-

bility constraints, and applies weighted edges to enumerate unique bearing angle measurements available to an observer. By applying Lie derivative results, it is determined that observer spacecraft may estimate their own orbits and their targets' orbits if the sum of edge weights directed to the observer's node is greater than or equal to the size of the observer's subgraph.

To numerically assess the achievable state uncertainty of an angles-only system, the observer state covariance is estimated using measurement sensitivity and noise matrices. The numeric method is augmented with new inclusions of time-varying physically correlated dynamics noise and partial measurement availability. Observability assessments for varying orbit geometries and estimated states reveal that observer clock offsets, differential ballistic coefficients and sensor biases are observable with angles-only measurements. Observability is strongest when target relative motion is highly nonlinear, geometrically distinct, and large in magnitude. The analytic observability conditions are verified numerically by computing the observability of all two- and three-spacecraft subsystems and remain consistent regardless of orbit geometry or dynamics model fidelity.

To automatically optimize angles-only observability, the analytic and numeric methods are placed wi-

thin a quasi-Newton optimization framework. A flexible cost function is developed to balance system costs with navigation performance. The PQN-BFGS method is applied for box-constrained optimization with an added exploration step to prevent convergence to non-convex local minima. Two case studies are explored: a distributed science swarm in low lunar orbit and a space situational awareness constellation in medium lunar orbit. Each converges to a global minimum for 50 random initializations and the optimal designs successfully fulfil navigation performance constraints under realistic measurement conditions. The method therefore demonstrates strong potential for automatic observability-aware design. Future research will investigate problem reformulation via a convex reduced-order observability model, to provide mathematical guarantees of reaching a globally optimal result, and treatment of other navigation architectures such as range-only methods.

Acknowledgements

This work is sponsored by the Air Force Office of Scientific Research (AFOSR) and Dr. Michael Yakes via award number FA9550-21-1-0414, for the project titled ‘Autonomous Distributed Angles-Only Orbit Determination using Multiple Observers’.

References

- [1] M. D. Johnston, D. Tran, B. Arroyo, S. Sorensen, P. Tay, B. Carruth, A. Coffman, and M. Wallace, “Automated Scheduling for NASA’s Deep Space Network,” *AI Magazine*, vol. 35, no. 4, pp. 7–25, 2014.
- [2] C. Underwood, S. Pellegrino, V. J. Lappas, C. P. Bridges, and J. Baker, “Using CubeSat/micro-satellite technology to demonstrate the Autonomous Assembly of a Reconfigurable Space Telescope (AAReST),” *Acta Astronautica*, vol. 114, pp. 112–122, 2015.
- [3] J. Sullivan, A. W. Koenig, J. Kruger, and S. D’Amico, “Generalized Angles-Only Navigation Architecture for Autonomous Distributed Space Systems,” *Journal of Guidance, Control, and Dynamics*, vol. 244, no. 6, pp. 1087–1105, 2021.
- [4] J. Kruger, K. Wallace, A. W. Koenig, and S. D’Amico, “Autonomous Angles-Only Navigation for Spacecraft Swarms around Planetary Bodies,” in *2021 IEEE Aerospace Conference*, (Big Sky, Montana), 2021.
- [5] H. Sanchez, D. McIntosh, H. Cannon, C. Pires, M. Field, J. Sullivan, S. D’Amico, and B. O’Connor, “Starling-1: Swarm Technology Demonstration,” in *32nd Annual Small Satellite Conference*, (Logan, UT), Aug. 2018.
- [6] J.-S. Ardaens and G. Gaias, “Angles-only relative orbit determination in low earth orbit,” *Advances in Space Research*, vol. 61, no. 11, pp. 2740–2760, 2018.
- [7] B. B. Reed, R. C. Smith, B. Naasz, J. Pellegrino, and C. Bacon, “The Restore-L Servicing Mission,” in *2016 AIAA Space Forum*, (Long Beach, California), 2016.
- [8] S. D’Amico, J.-S. Ardaens, G. Gaias, H. Benninghoff, B. Schlepp, and J. L. Jørgensen, “Non-cooperative Rendezvous Using Angles-Only Optical Navigation: System Design and Flight Results,” *Journal of Guidance, Control, and Dynamics*, vol. 36, pp. 1576–1595, Nov. 2013.
- [9] A. W. Koenig, J. Kruger, and S. D’Amico, “ARTMS: Enabling Autonomous Distributed Angles-Only Orbit Estimation for Spacecraft Swarms,” in *American Control Conference*, (New Orleans, Louisiana), 2021.
- [10] K. Iiyama, J. Kruger, and S. D’Amico, “Autonomous Distributed Angles-Only Navigation and Timekeeping in Lunar Orbit,” in *ION International Technical Meeting*, (Long Beach, California), 2022.
- [11] A. W. Koenig and S. D’Amico, “Observability-Aware Numerical Algorithm for Angles-Only Initial Relative Orbit Determination,” in *2020 AAS/AIAA Astrodynamics Specialist Conference*, (Lake Tahoe, California), 2020.
- [12] Y. Hu, I. Sharf, and L. Chen, “Three-spacecraft autonomous orbit determination and observability analysis with inertial angles-only measurements,” *Acta Astronautica*, vol. 170, pp. 106–121, 2020.
- [13] Y. Hu, I. Sharf, and L. Chen, “Distributed orbit determination and observability analysis for satellite constellations with angles-only measurements,” *Automatica*, vol. 129, 2021.

- [14] D. C. Woffinden and D. K. Geller, "Observability Criteria for Angles-Only Navigation," *IEEE Transactions on Aerospace and Electronic Systems*, vol. 45, no. 3, pp. 1194–1208, 2009.
- [15] J. Hippelheuser and T. A. Elgohary, "Inertial space-based orbit estimation: A new measurement model for multiple observers," *Acta Astronautica*, vol. 181, 2021.
- [16] R. T. Nallapu and J. Thangavelautham, "Towards End to End Design of Spacecraft Swarms for Small-Body Reconnaissance," in *70th International Astronautical Congress*, (Washington, USA), 2019.
- [17] D. A. Vallado and W. D. McClain, *Fundamentals of Astrodynamics and Applications*. Hawthorne, California: Microcosm Press, 4 ed., 2013.
- [18] S. D'Amico, *Autonomous Formation Flying in Low Earth Orbit*. PhD Thesis, Delft University, 2010. OCLC: 839641932.
- [19] A. W. Koenig, T. Guffanti, and S. D'Amico, "New State Transition Matrices for Relative Motion of Spacecraft Formations in Perturbed Orbits," *Journal of Guidance, Control, and Dynamics*, Sept. 2016.
- [20] R. L. Cognion, "Large phase angle observations of GEO satellites," in *Sensors and Systems for Space Applications VI* (K. D. Pham, J. L. Cox, R. T. Howard, and G. Chen, eds.), vol. 8739, pp. 194–205, International Society for Optics and Photonics, SPIE, 2013.
- [21] K. T. Alfriend, ed., *Spacecraft Formation Flying: Dynamics, Control, and Navigation*. Elsevier astrodynamics series, Oxford: Butterworth-Heinemann/Elsevier, 2010. OCLC: 699265912.
- [22] D. Brouwer, "Solution of the problem of artificial satellite theory without drag," *Astronomical Journal*, vol. 64, no. 1274, pp. 378–397, 1959.
- [23] T. Guffanti and S. D'Amico, "Linear models for spacecraft relative motion perturbed by solar radiation pressure," *Journal of Guidance, Control, and Dynamics*, pp. 1–20, 2019.
- [24] L. Galleani, L. Sacerdote, P. Tavella, and C. Zucca, "A mathematical model for the atomic clock error," *Metrologia*, vol. 40, pp. 257–264, 2003.
- [25] T. Boukhobza and F. Hamelin, "Observability analysis for structured bilinear systems: A graph-theoretic approach," *Automatica*, pp. 1968–1974, 2007.
- [26] R. Sharma, R. Beard, C. Taylor, and S. Quebe, "Graph-based observability analysis of bearing-only cooperative localization," *IEEE Transactions on Robotics*, vol. 28, no. 2, pp. 522–529, 2012.
- [27] R. Hermann and A. J. Krener, "Nonlinear Controllability and Observability," *IEEE Transactions on Automatic Control*, vol. 22, no. 5, pp. 728–740, 1977.
- [28] M. Chernick and S. D'Amico, "New Closed-Form Solutions for Optimal Impulsive Control of Spacecraft Relative Motion," *Journal of Guidance, Control, and Dynamics*, vol. 41, no. 2, pp. 301–319, 2018.
- [29] J. Sullivan and S. D'Amico, "Nonlinear Kalman Filtering for Improved Angles-Only Navigation Using Relative Orbital Elements," *Journal of Guidance, Control, and Dynamics*, pp. 1–18, July 2017.
- [30] P. Misra and P. Enge, *Global Positioning System: Signals, Measurements, and Performance*. Lincoln, Massachusetts: Ganga-Jamuna Press, 2011.
- [31] S. K. Singh, R. Woollands, E. Taheri, and J. Junkins, "Feasibility of quasi-frozen, near-polar and extremely low-altitude lunar orbits," *Acta Astronautica*, vol. 166, pp. 450–468, 2020.
- [32] L. McManus and H. Schaub, "Establishing a formation of small satellites in a lunar flower constellation," *Advances in the Astronautical Sciences*, vol. 63, pp. 263–286, 2016.
- [33] R. Fletcher, *Practical Methods of Optimization*. Hoboken, New Jersey: John Wiley & Sons, 1987.
- [34] D. Kim, S. Sra, and I. S. Dhillon, "Tackling Box-Constrained Optimization via a New Projected Quasi-Newton Approach," *SIAM J. Sci. Comput.*, vol. 32, pp. 3548–3563, 2010.
- [35] Y. N. Dauphin, R. Pascanu, C. Gulcehre, K. Cho, S. Ganguli, and Y. Bengio, "Identifying and attacking the saddle point problem in high-dimensional non-convex optimization," in

REFERENCES

Advances in Neural Information Processing Systems (Z. Ghahramani, M. Welling, C. Cortes, N. Lawrence, and K. Weinberger, eds.), vol. 27, Curran Associates, Inc., 2014.

REFERENCES